Fragmentation Patterns and Trajectories During Rockfall: Analysis of the Influence of Discontinuities and Impact Conditions Through Drop Tests

Rock Mechanics and Rock Engineering
https://doi.org/10.1007/s00603-025-04937-3

ORIGINAL PAPER

Fragmentation Patterns and Trajectories During Rockfall: Analysis of the Influence of Discontinuities and Impact Conditions Through Drop Tests

Maddalena Marchelli[1] · Davide Ettore Guccione[2] · Anna Giacomini[2] · Olivier Buzzi[2]

Received: 27 May 2025 / Accepted: 2 September 2025

Abstract

Fragmentation of rock blocks upon impact with the slope is a common occurrence during rockfall events. This process entails the division of an initial rock block either through breakage into new fragments or through the disaggregation of blocks that are weakly bound by cohesion or cementation, or a combination of both mechanisms. Despite significant advancements in understanding and predicting rockfall occurrences and their propagation, the fragmentation of rock blocks during impact remains underexplored. Existing experimental and numerical studies on the fragmentation of brittle materials under controlled conditions have provided valuable insights into the breakage of intact rock at a meso-scale. However, the effects of pre-existing discontinuities on the fragmentation process, the size distribution of fragments, and their trajectories, have not been sufficiently addressed. The current research focuses on an experimental campaign of vertical drop tests, where discontinuities are artificially introduced into spheres of mortar. Series of discontinuity patterns are examined to understand how their geometrical configuration (encompassing their number and position within the block and inclination with respect to the impacted surface) along with the impact velocity, influence fragmentation mechanisms. Fracture patterns, fragments masses, and trajectories are analysed in detail through image analysis. The results reveal that the geometrical configuration of the discontinuities within the sample affects the size and number of the fragments. Additionally, the inclination of the discontinuity planes relative to the impacted surface, along with the impact velocity, determines the probability and type of breakage, as well as the trajectories of the fragments.

Highlights

- Data from 442 drop tests of mortar spheres with discontinuities were analysed to study the effect of discontinuity patterns and impact conditions on fragmentation.
- The fracture patterns and fragment trajectories depend on the impact velocity and the position of the discontinuity plane(s) relative to the impacted surface.
- According to the impact velocity and impact angle, predefined orientations of the fragments were highlighted.
- In all the investigated cases, a normal restitution coefficient of less than 0.3 was observed.

Keywords Fragmentation processes · Fracture pattern · Fragment size · Rockfall trajectories · Rock joints · Drop tests

✉ Maddalena Marchelli
maddalena.marchelli@polito.it

Davide Ettore Guccione
davide.guccione@newcastle.edu.au

Anna Giacomini
anna.giacomini@newcastle.edu.au

Olivier Buzzi
olivier.buzzi@newcastle.edu.au

[1] Department of Environment, Land and Infrastructure Engineering, Politecnico di Torino, Corso Duca degli Abruzzi, 24, 10129 Tourin, Italy

[2] Centre for Geotechnical Science and Engineering, The University of Newcastle, University Dr, Callaghan, NSW 2308, Australia

Published online: 26 September 2025

1 Introduction

Rockfall events pose significant risks to infrastructure, human life, and the environment (Scavia et al. 2020; Hantz et al. 2021; Rosser and Massey 2022). Over the past decades, research has advanced in identifying detachment zones and volume-frequency relationships (Mavrouli et al. 2015; Graber and Santi 2022; Moos et al. 2022), modelling propagation (Wyllie 2014; Leine et al. 2014; Li and Lan 2015; Asteriou and Tsiambaos 2018; Noël et al. 2022; Dorren et al. 2023), assessing hazard and risk(Crosta and Agliardi 2003; Ferrari et al. 2016; Marchelli et al. 2022), monitoring (Williams et al. 2019; Giacomini et al. 2020; Blahůt and Racek 2023), and designing mitigation measures (Jaccard et al. 2020; Marchelli et al. 2023).

Fragmentation during rockfall, whether through breakage of intact blocks or disaggregation along discontinuities, has been frequently observed (Corominas et al. 2017; De Blasio and Crosta 2015), and it significantly influences fragment size distribution and post-impact trajectories (Ruiz-Carulla et al. 2017; De Biagi 2017; Marchelli and De Biagi 2019). Researchers in the field have shown that rock fragmentation is primarily influenced by the shape and size of the impacting rock, its impact velocity and impact angle with respect to the impacted surface, as well as the presence and orientation of discontinuities (Giacomini et al. 2009; Wang and Tonon 2011a; Lin et al. 2020; Azadmehr et al. 2019; Azizi and Moomivand 2021). However, the inherent variability in rock material properties, block shapes, and natural structural conditions makes fragmentation one of the most challenging aspects of rockfall analysis, and despite its importance, it remains underexplored, particularly regarding the role of pre-existing discontinuities. As a result, researchers have primarily investigated fragmentation mechanisms under controlled conditions. Notable examples include experimental (Arbiter 1969; Shipway and Hutchings 1993b, a; Tomas et al. 1999; Wu et al. 2004; Salman et al. 2003, 2004; Guccione et al. 2021a, 2023) and numerical (Khanal et al. 2004a, b; Carmona et al. 2008; Wittel et al. 2008) studies using artificial brittle spheres subjected to static and dynamic loading. These works have provided valuable insights into fracture processes.

Failure typically initiates at the impact point along a conical surface, known as the compressive cone, often covered by pulverized material (Arbiter 1969; Tomas et al. 1999; Wu et al. 2004; Khanal et al. 2004a). Tensile cracks then propagate from this surface, forming meridian fracture planes along the loading axis. As impact energy increases, more meridian cracks develop, dividing the sphere into wedge-shaped fragments resembling "orange slices" (Tomas et al. 1999; Wu et al. 2004). Oblique fractures may also form along paths of maximum compression due to divergent stress waves. At higher energies, internal shear and surface tensile cracks appear, especially on elastic targets (Shipway and Hutchings 1993b, a; Tomas et al. 1999), producing wedge- and lune-shaped fragments with angular distributions linked to impact energy (Carmona et al. 2008; Wittel et al. 2008; Guccione et al. 2023). At very high energies, a top cone may also form (Wu et al. 2004; Guccione et al. 2023). Regarding fragmentation probability, Guccione et al. (2021a) have proposed a model predicting the survival of brittle spheres without discontinuities during free fall, based on the statistical distribution of material properties. This model has been later extended to irregular rock shapes under collinear impact (Buzzi and Guccione 2023).

Numerical models have been developed (Khanal et al. 2004a; Carmona et al. 2008; Wittel et al. 2008; Liu et al. 2010; Wang and Tonon 2011a; Zhao et al. 2017; Ye et al. 2019, 2021; Liu et al. 2021; Buzzi et al. 2024; Wu et al. 2025) to investigate fragmentation mechanisms, fragment size distributions, and energy dissipation upon impact. Carmona et al. (2008) and Wittel et al. (2008) have observed that smaller fragments follow a power-law distribution, while larger ones conform to a two-parameter energy-dependent Weibull distribution, with local maxima linked to meridian crack formation.

However, these studies focus on homogeneous materials and largely overlook the role of pre-existing discontinuities, which has only been addressed in a limited number of investigations. Aziznejad et al. (2018) have showed that joints significantly affect stress wave propagation and energy dissipation in jointed meta-sandstone. Similarly, Wu et al. (2019) have found that joints, especially if filled, reduce transmitted wave peaks and interrupt crack propagation. Butcher et al. (2021) have demonstrated that in laminated travertine, critical drop height for failure decreases by a factor of two to four when laminations are inclined between 45° and 90° to the impact surface. Field-scale rockfall tests (Giacomini et al. 2009; Gili et al. 2018; Ruiz-Carulla et al. 2020; Gili et al. 2022; Prades-Valls et al. 2022) have further highlighted the role of weakness planes, impact conditions, and material properties in controlling fragmentation patterns and fragment trajectories. Notably, Giacomini et al. (2009) have emphasized the dominant influence of impact angle over energy, while Gili et al. (2022) linked breakage probability to incidence angle, contact geometry, and lithology, rather than to a fixed energy threshold.

However, in-situ fragmentation data remain scarce in the literature, likely due to the technical challenges involved in conducting such tests. Observations from real cases suggest that fragment size distributions often follow a power law (Lanfranconi et al. 2024). To the authors' knowledge, no prior studies have examined the fracture patterns of brittle materials with discontinuities upon impact onto a planar

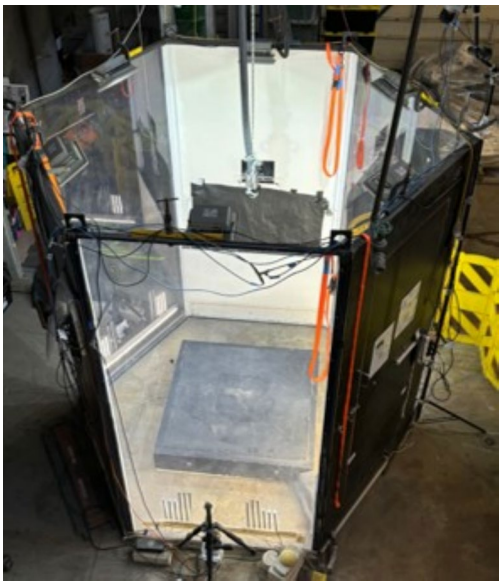

Fig. 1 Fragmentation cell developed at the University of Newcastle

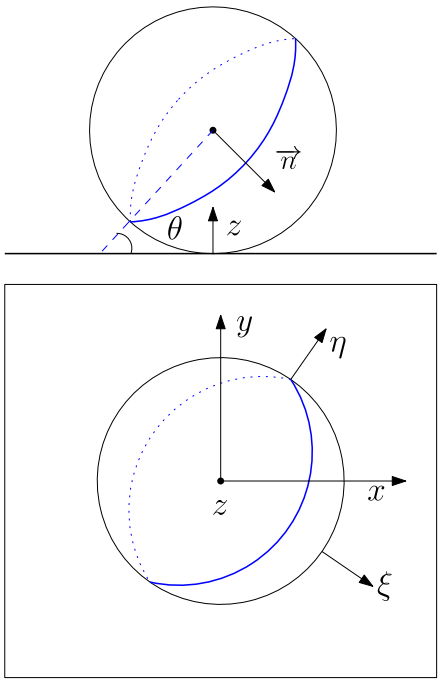

Fig. 2 Sketch of the local reference system. A 1–2Ds sphere is taken as an example. The outline of the discontinuity is marked in blue

surface. Given the similarities in fracture behaviour under static and dynamic loading for homogeneous brittle materials (Arbiter 1969; Shipway and Hutchings 1993b), existing studies on tensile or shear-tensile failure in jointed rocks under static loads offer a valuable starting point for understanding failure mechanisms under impact. Han et al. (2022) have found that tensile resistance is lowest when a discontinuity aligns with the loading axis, with cracks initiating within the joint, while a plateau near the tensile strength of intact rock is observed when the discontinuity is inclined at 45°. Both Han et al. (2022) and Xu et al. (2024) have demonstrated a transition in failure modes as the angle between the discontinuity and the loading axis varies from 0° to 90°, including tensile failure along the discontinuity, tensile-shear composite failure, shear failure, and tensile failure in the intact rock.

Beyond understanding fragmentation mechanisms, incorporating fragment kinematics into trajectory models is essential for accurately predicting post-impact paths. Recently, Corominas and colleagues (Matas et al. 2017, 2020; Ruiz-Carulla and Corominas 2020; Ruiz-Carulla et al. 2021) proposed two complementary models: one predicting fragment size distributions based on detachment volumes, and another lumped-mass trajectory model incorporating fragmentation, validated through full-scale tests. Despite their value, these models rely on key assumptions that highlight existing knowledge gaps: fragmentation probability is treated as random (0 1), kinetic energy is distributed by fragment mass, and trajectories are confined within a cone of arbitrarily defined aperture. An alternative model by Wang and Tonon (2011a), later extended by Wang and Tonon (2011b), Frattini et al. (2012), Lanfranconi et al. (2023), accounts for fragmentation when impact energy exceeds a Weibull-based threshold. However, it requires several site-specific parameters (e.g., Young's modulus, Poisson's ratio, UCS, block volume, Weibull parameters), making calibration difficult. As in Matas et al. (2017), fragment energy is proportional to mass, and ejection directions are stochastically assigned within a cone defined by a model input.

A thorough understanding of fragmentation mechanisms and their evolution upon impact is essential for improving predictive models used in rockfall hazard assessment and the design of mitigation measures. This study addresses the current knowledge gaps by experimentally investigating under controlled impact conditions the fragmentation behaviour of brittle materials containing pre-existing discontinuities. To this end, a large-scale drop test campaign was conducted using spherical specimens with artificial fully persistent planar discontinuities, systematically varying their number, position, inclination with respect to the impact surface, as well as the impact velocity. The analysis focuses on how these parameters influence fracture initiation and propagation, fragment size distribution, and post-impact trajectories. The findings aim to enhance the physical realism of rockfall models and contribute to more accurate risk assessments and mitigation strategies.

The experimental methodology is presented in Sect. 2, which describes the experimental setup (Sect. 2.1), the materials and specimens used (Sect. 2.2), and the experimental program (Sect. 2.3). The results are discussed in

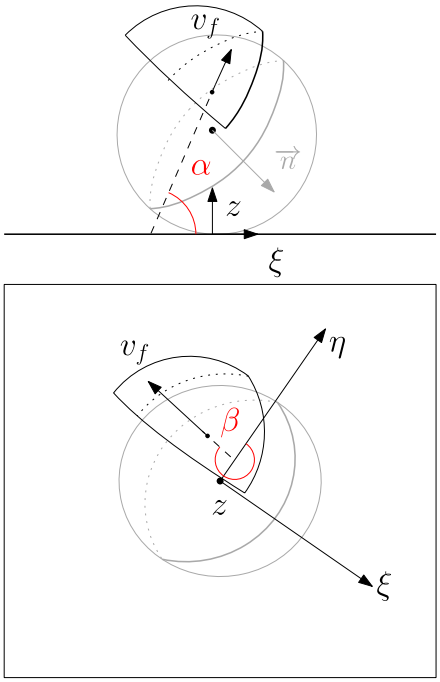

Fig. 3 Sketch of a post-impact fragment with its velocity vector, highlighting the angles α (front view, top part of the figure) and β (plane view, bottom part of the figure). As an example, a sphere containing a central planar discontinuity is considered, with only one resulting fragment illustrated for clarity. The intact sphere prior to impact is outlined in grey

Sect. 3, beginning with the definition of fragmentation patterns (Sect. 3.1), followed by an analysis of the influence of impact parameters and discontinuity configurations on fragmentation patterns (Sect. 3.2), fragment number and size distribution (Sect. 3.3), and fragment trajectories (Sect. 3.4). Finally, conclusions and future perspectives are provided in Sect. 4.

2 Experimental Method

2.1 Experimental Setup

Series of vertical drop tests were conducted in the fragmentation facility designed at the University of Newcastle (Guccione et al. 2021b) (Fig. 1). The facility is an enclosed hexagonal container equipped with an instrumented fibre reinforced concrete slab, a vacuum-based release system and a sophisticated image recording system (for details refer to Guccione et al. 2021b) of 6 high-speed cameras allowing the recording of spheres' free-falling phase, their impact and VEO-E340L high-speed cameras were added to the original setup, which included four Optronics cameras, all positioned outside the cell. The cameras captured images at a rate of 500 frames per second, with exposure times of 500 μs for the Optronics cameras and 100 μs for the Phantom cameras. The samples were positioned in the vacuum releasing mechanism in such a way to achieve at the impact various inclinations of the discontinuity with respect to the slab.

The motion of the fragments created upon impact is processed using the commercial software TEMA3Ds (TEMA 2019) according to the calibration procedure described by Guccione et al. (2021b), for which the 3Ds trajectories of any rotating irregular fragment are tracked using an outline tracking algorithm that reconstructs the shape of a 3Ds object from silhouettes captured from different views. Drop tests with artificial spheres including different discontinuities configurations are conducted with no initial rotation. All fragments were recorded, collected and weighted. Only fragments with mass larger than 15 g, approximately 1.5% of the initial mass, that experienced rebound were tracked until they were visible from at least two cameras or impacted the slab, or other fragments. Sliding and rolling fragments were not tracked.

Tracked tests were post-processed in the Matlab environment (The MathWorks Inc. 2023) to analyse fragment sizes and trajectories, and to examine their correlation with impact conditions and discontinuity configurations. The x, y, z global reference system used to track the fragments was centred at the middle of the slab, i.e., the impact plane, with the x y axes lying on the slab surface and the z axis oriented normal to it. To analyse the results consistently and ensure directional comparability, all obtained velocity vectors were rotated from the $x-y$ plane in the global reference system to a local $\xi-\eta$ plane centred at the sphere's centre of gravity. The ξ-axis represents the projection on the $x-y$ plane of the unit vector $\vec{n}$ normal to the discontinuity plane pointing towards the slab. In the present study, configurations

Table 1 Characteristics of mortar mixtures. The values are presented as averages, with standard deviations indicated. The abbreviations 'sec' and 'tan' denote secant and tangent, respectively. The third row report the ratio of the mean strength values

Material	Proportions: sand/cement/lime/water	Young modulus (tan) (MPa)	Young modulus (s) (MPa)	Unconfined compressive strength σ_c (MPa)	Tensile strength σ_t (MPa)	Fracture toughness K_{Ic} (MPa·m$^{1/2}$)
Matrix	3/1/0.125/1	2050±223	1345±265	16.62±1.62	2.00±0.18	0.4393±0.090
Filling	3.5/0.8/1/1.2	1201±172	731±170	8.47±2.03	1.06±0.21	0.181±0.016
$\frac{Filling}{Matrix}$		0.58	0.54	0.51	0.53	0.41

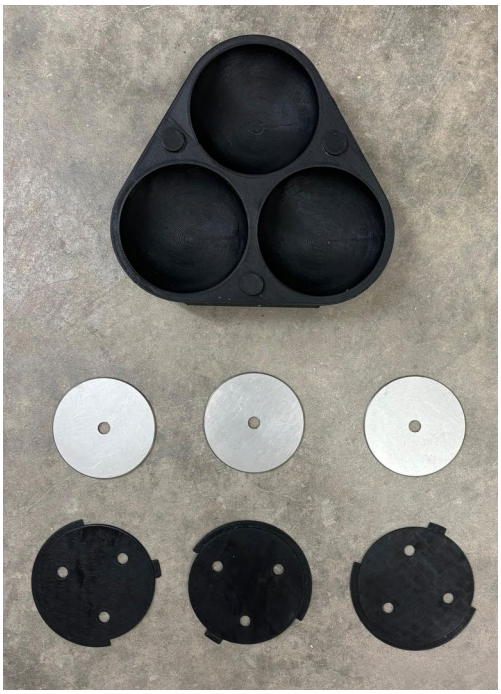

Fig. 4 High-density Acrynitrile Butadiene Styrene moulds and discs (in Acrynitrile Butadiene Styrene and steel) used to create the spheres and the partitions inside them

with multiple discontinuities feature parallel planes. The η axis, normal to the ξ axis, lies on the $x-y$ plane, positive clockwise from ξ. Being $\frac{\pi}{2}-\theta$ the angle between $\vec{n}$ and the plane of the slab, the unit vector $\vec{i_\xi}$ on the ξ-axis could be obtained considering:

$$\vec{n}\cdot\vec{i_\xi}=\sin\theta. \tag{1}$$

As the impact takes place near the centre of the slab, coinciding with the origin of the global reference frame, no translation to a local coordinate system is necessary. Thus, the z-axis is aligned in both the global and local reference systems. This procedure allows for the comparison of the post-impact directions of the fragments with respect to the plane of the discontinuity. Figure 2 shows the scheme of the adopted reference system.

The planar angle β, measured clockwise between the η-axis and the velocity vector, was defined to analyse the distribution of velocity vector directions on the $\xi\,\eta$ plane. Trajectories aligned with the positive ξ-axis direction thus exhibit $\beta\approx 90°$. Additionally, the angle α between the vertical component (v_z) and the horizontal components (v_ξ and v_η, combined as $\sqrt{v_\xi^2+v_\eta^2}$) of the post-impact fragment velocity was examined to quantify the vertical projection of the fragment's motion. Both angles are illustrated in Fig. 3.

2.2 Material and Specimen Preparation

The mortar is composed of silica sand, Portland cement, hydrated lime and water in a 3:1: 0.125: 1 mass ratio, with a cement accelerant (2% by weight of cement) added to speed up curing. This results in a density of approx 2000 kg/m^3 when dried. The use of a fixed spherical shape and mortar material is intended to minimize natural rocks variability and work within controlled conditions.

The spheres were cast in 3Ds printed moulds made of high-density Acrylonitrile Butadiene Styrene (Fig. 4). To create the discontinuities, different portions of the spheres were created first, and then glued together. A homogeneous 2 to 4 mm thick infill was used for the discontinuities. After preparation, the spheres were cured for 2 weeks in a 100% humid environment and then dried for 3 weeks in an oven set at 40°C. The vertical drop tests were performed immediately after the curing process. Since the samples were cast in different batches, material characterization tests, i.e., brazilian (BT) (Bieniawski and Hawkes 1978), unconfined compressive (UCS) (Bieniawski and Bernede 1979), and toughness (Kuruppu et al. 2014) tests, were carried out for each batch. A total of 121 BT, 131 UCS and 136 toughness tests were performed. Table 1 reports the obtained values.

To simulate natural rock discontinuities, typically unfilled or soil-infilled and often only slightly consolidated, a weaker mortar was used to fill the artificial joints. This material had approximately half the compressive and tensile strength of the mortar used for the main body of the sphere, as reported in Table 1. This strength contrast was selected to reflect realistic conditions in which discontinuities act as mechanical weaknesses. Particular attention was given to the tensile strength of the joint material, as it plays a critical role in the initiation and propagation of fractures along discontinuities (Shang et al. 2016), although the shear strength and the adhesion of the interface are also acknowledged as an important factors in the overall fragmentation process. The mortar used for the discontinuities includes sand, cement, hydrated lime, and water ratio of 3.5:0.8:1:1.2 by mass. A total of 71 BT, 63 UCS and 69 toughness tests were performed for this mortar and the resulting properties are listed in Table 1.

2.3 Experimental Program

The experimental campaign was designed to investigate how internal discontinuities and impact characteristics influence the fragmentation behaviour of brittle materials under controlled conditions. Specifically, it aimed to assess the effect of discontinuity geometry, namely the number, position, and spacing, as well as the role of impact conditions, such as impact velocity and the inclination of the discontinuity plane relative to the impacted surface. Spheres with a diameter of 100 mm were selected to enable comparison

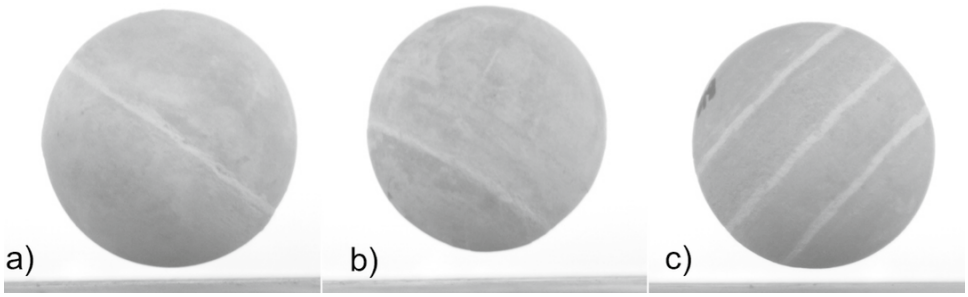

Fig. 5 **a** 1–2Ds sphere (i.e. discontinuity in the middle of the sphere), **b** 1–4Ds sphere (i.e. discontinuity at 1/4 of the sphere diameter), **c** 3Ds sphere (3 parallel discontinuities at 1/4, 1/2, 3/4 of the sphere. All the photos are intended in front view, being the impact plane horizontal

with previous studies on brittle intact spheres (Guccione et al. 2021a, 2023), which also included 50 mm and 75 mm specimens. Among these, the 100 mm size provided more detailed insights and a broader dataset. Since probability of no breakage tends to increase with diameter at a given impact velocity (Guccione et al. 2021a), and the presence of discontinuities is expected to promote breakage, using larger spheres allowed us to also investigate non-breakage scenarios. Additionally, 100 mm specimens are more practical for inserting artificial discontinuities with precision.

Three different discontinuity configurations were selected: one with a single planar discontinuity through the sphere's centre (named '1–2Ds' series, Fig. 5a), one with a single discontinuity offset at one-quarter of the diameter (named '1–4Ds' series, Fig. 5b), and and one with three equally spaced parallel discontinuities at 1/4, 1/2, and 3/4 of the diameter of the sample (named '3D' series, Fig. 5c). These configurations were chosen to represent varying joint densities (1–2Ds and 3Ds) and joint spacing, which affects the distance between the discontinuity and the impact surface (1–2Ds vs. 1–4Ds), both of which are commonly observed in natural rock masses.

In addition to discontinuity geometry, impact conditions, specifically impact velocity and the inclination of the discontinuity plane relative to the impacted surface, are known to play a critical role in fragmentation processes. To investigate these effects, a range of impact velocities and inclinations was tested for each configuration. The velocity ranges were iteratively adjusted during the campaign to span different survival probabilities, as defined by Guccione et al. (2021a), who reported that homogeneous 100 mm spheres exhibit survival probabilities of 100% at velocities ≤5 m/s, 50% at 6 m/s, and 0% at higher velocities. The number of tests was determined based on the findings of Guccione et al. (2021a), who reported that approximately 10 tests are sufficient for the survival probability to stabilize in 100 mm spheres without discontinuities. Building on this, a minimum of 20 tests was conducted at velocities of 6, 7, and 10 m/s (corresponding to drop heights of 1.84, 2.50, and 5.10 m, respectively), where breakage is expected in more than 50% of intact samples. Additional tests at lower velocities were included in the 1 2D and 3D series, starting from 5 m/s (drop height of 1.27 m) for the 1 2D series and 3 m/s (drop height of 0.5 m) for the 3D series with higher joint density. These tests aimed to capture the increased likelihood of breakage due to discontinuities and to support a parallel study on survival probability. Cases in which the survival probability differs from 0% will be addressed in future research, as this topic lies beyond the scope of the present study. A smaller set of 15 tests was also performed on the 1–2Ds series at 8.5 m/s (drop height of 3.68 m) to assess behavioural variability across velocities in samples containing a single discontinuity.

A total of 442 samples were prepared and tested: 190 with a central discontinuity, 75 with an off-centre discontinuity, and 177 with multiple parallel discontinuities. Table 2 reports the investigated velocities and number of samples.

Different inclinations of the discontinuity set relative to the slab were achieved as described in Sect. 2.1. Denoting this angle as θ, the inclination values were systematically classified into discrete categories, hereinafter referred to as 'impact angle categories'. Three impact angle categories were defined for the 1–2Ds series (Fig. 6a), while four for the 1–4Ds (Fig. 6b) and 3Ds (Fig. 6c) series. For the 1–2Ds series, the groups were selected as $\theta = 0° \pm 15°$, $\theta = 45° \pm 29°$, and $\theta = 90° \pm 15°$. For the 1–4Ds series, a distinction was made for the $\theta = 45° \pm 29°$ case, indicating with the letter *b* and *t*, standing for 'bottom' and 'top', the position of the discontinuity with respect to the impact surface, as highlighted in Fig. 6b). To ease the notation, from here on, each impact angle category is recalled as the mean angle between the discontinuity and the slab only (hence neglecting the range). For the 3Ds series, a different grouping was applied to observe how fragmentation patterns and fragment trajectories changed depending on whether the impact occurred within the discontinuities or at one of the discontinuities. In this case, four impact angle categories were considered, namely 'Before 1' (i.e. $\theta <\approx 60°$), 'On 1' (i.e. $\theta \approx 60°$), 'Between 1 &2' (i.e. $\theta >\approx 60°$ and $\theta <\approx 90°$), and 'On 2' (i.e. $\approx 90°$). The term '1' refers to the discontinuity located at either 1/4 or 3/4 of the diameter, due to symmetry, while '2' to the discontinuity at 1/2 of the sphere, only. The number of tests for each group is included in Table 2.

Table 2 Summary of test parameters. "Imp. ang. cat." stands for impact angle category. For the 3Ds samples, A = Before 1, B = On 1, C=Between 1 &2, D=On 2

1–2Ds															
Velocity	5 m/s			6 m/s			7 m/s			8.5 m/s			10 m/s		
Imp.ang. cat.	0°	45°	90°	0°	45°	90°	0°	45°	90°	0°	45°	90°			
N°(-)	7	33	10	12	27	14	10	29	13	2	11	2	5	6	9
Total n°(-)	50			53			52			15			20		
1–4Ds															
Velocity	6 m/s				7 m/s				10 m/s						
Imp.ang. cat.	0°	45*t*°	90°	45*b*°	0°	45*t*°	90°	45*b*°	0°	45*t*°	90°	45*b*°			
N°(-)	5	7	6	6	3	11	5	6	4	12	5	5			
Total n°(-)	24				25				26						
3Ds															
Velocity	3 m/s				4 m/s				5 m/s				6 m/s				7 m/s			
Imp.ang. cat.	A	B	C	D	A	B	C	D	A	B	C	D	A	B	C	D	A	B	C	D
N°(-)	26	0	5	11	24	5	4	8	30	11	4	6	10	8	1	3	10	7	1	3
Total n°(-)	42				41				51				22				21			

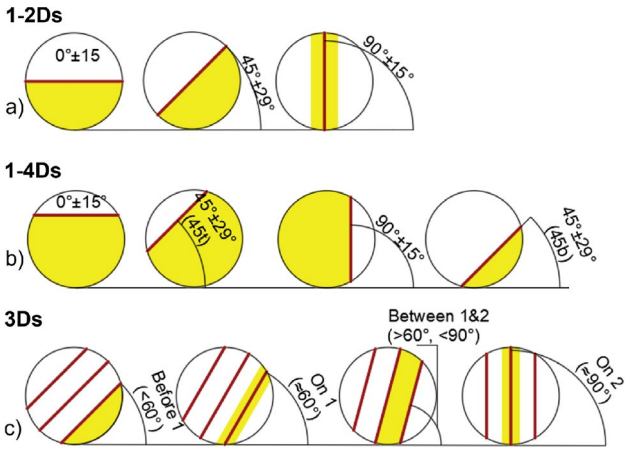

Fig. 6 Impact angle categories for **a** 1–2Ds, **b** 1–4Ds, **c** 3Ds. A yellow area highlights the zone in which the impact occurs, while a red line highlights the position of the discontinuity(ies). All the sketches are intended in front view, being the slab on the horizontal plane

After each test, all the fragments were labelled, weighted and stored in such a way to be recognizable during the image processing and post-processing.

3 Results and Discussion

3.1 Fragmentation Patterns: Proposed Nomenclature

Images from the high-speed cameras were used to identify the fragmentation patterns. In the following, the nomenclature used to describe the fragmentation pattern is reported. Table 3 summarizes all the observed patterns, while Figs. 7 and 8 report photographic examples. When the influence of the discontinuity is negligible, the identification of fracture modes and the proposed nomenclature align with the findings of previous studies on spheres without discontinuities (named as homogeneous in the following) (Arbiter 1969; Shipway and Hutchings 1993b, a; Tomas et al. 1999; Salman et al. 2003, 2004; Wu et al. 2004; Khanal et al. 2004a, b; Carmona et al. 2008; Wittel et al. 2008; Guccione et al. 2023): (i) meridian (M), where a single meridian fracture occurs, splitting the sphere in a tensile mode (Fig. 7a); (ii) orange slices (O), where multiple meridian fractures occur with possible secondary oblique plane cracks (not along the discontinuity/ies) (Fig. 7b); (iii) orange slices with top cone (OTC), where a significant top cone fragment forms along with a bottom cone (Fig. 7c). In the O case, the fragments resemble orange slices or wedges if oblique cracks are present; in the OTC case, 'lune-shaped' fragments form around the cone. A bottom cone at the impact point can form in any case.

When one or more discontinuities influence the fragmentation pattern, the following observed patterns are proposed: (i) parallel disaggregation (PD), when the sphere separates solely along the discontinuities (Fig. 8a–c); (ii) meridian and parallel disaggregation (M+PD), when a single meridian fracture initiates at the slab-sphere impact point, with additional fractures along the discontinuities (Fig. 8d–f); (iii) orange slices and parallel disaggregation (O+PD), when meridian fractures begin at the slab-sphere impact point, accompanied by fractures along the discontinuities (Fig. 8g–i); (iv) orange slices with top cone and parallel disaggregation (OTC+PD), when a prominent top cone fragment forms alongside 'lune-shaped' fragments, with fractures also occurring along the discontinuities (Fig. 8j, k). If more than one discontinuity is present, the number of fractures, always along discontinuities, is added after PD, e.g. PD1,....PD*n*. For M+PD, O+PD, and OTC+PD, the occurrence of meridian cracks and parallel disaggregation depend on the impact angle relative to the discontinuity(ies), the position of the discontinuity(ies) within the block, and the impact velocity. Specifically: (a) both meridian cracks and parallel disaggregation may fully occur (Fig. 8i–k), or (b) either meridian (Fig. 9a) (c) or parallel disaggregation (Fig. 9b), (d) or both may be incomplete (Fig. 9c).

It is important to note that when a fracture forms along a discontinuity, no distinction is made between whether it occurs within the filling or along the interface between the two mortars.

3.2 Qualitative Fragmentation Mechanisms and Patterns Analysis

Drop tests data were analysed by considering impact velocities and positions. For each series, Table 4 displays the percentage associated to each observed fragmentation pattern and the samples that survived the impact (referred to as 'Intact'), categorized by impact velocities and further subdivided by impact angle category.

3.2.1 1–2Ds Series

For the 1–2Ds configuration, as expected, an increase in the impact velocity from 5 m/s to 7 m/s corresponds to a reduction in the percentage of samples remaining intact. For $v_i > 7$ m/s all samples break at impact. At 0°, the influence of the discontinuity appears negligible up to 7 m/s, for which instances of meridian cracks only (M or O) associated to tensile failure can be observed. Additional general observations can be made:

Table 3 Description and sketches of the fragmentation patterns. A single-discontinuity case is taken as an example. The double line represents the two faces of the discontinuity. (n) represents the number of involved discontinuities

Fragm.pattern	Description	Sketch
Fragmentation patterns that are not affected by the discontinuity(ies)		
M	Meridian: single meridian crack along the loading axis. A bottom cone can also be present	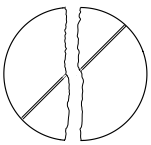
O	Orange slices: multiple meridian cracks along the loading axis with possible oblique secondary cracks. A bottom cone can also be present	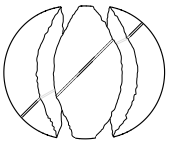
OTC	Orange slices with top cone: multiple meridian cracks along the loading axis (with possible oblique secondary cracks) and a top cone. A lower cone is present, which eventually connects to the upper cone, forming an hourglass-type shape	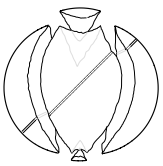
Fragmentation patterns that are affected by the discontinuity(ies)		
PD(n)	Parallel disaggregation(s): crack/s along the discontinuity(ies) only	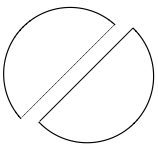
M+PD(n)	Meridian plus parallel disaggregation(s): single meridian crack along the loading axis and crack/s along the discontinuity(ies). A bottom cone can also be present	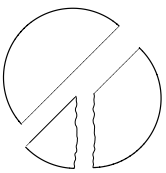
O+PD(n)	Orange slices plus parallel disaggregation(s): multiple meridian cracks along the loading axis (with possible oblique secondary cracks), and crack/s along the discontinuity(ies). A bottom cone can also be present	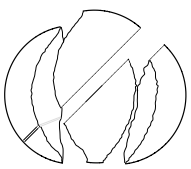
OTC+PD(n)	Orange slices with top cone plus parallel disaggregation(s): multiple meridian cracks along the loading axis (with possible oblique secondary cracks), top cone, and crack/s along the discontinuity(ies). A lower cone is present, which eventually connects to the upper cone, forming an hourglass-type shape	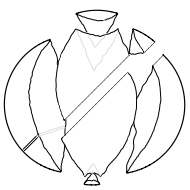

- when the impact point lies on the discontinuity ($\theta = 90°$), fragmentation occurs along the discontinuity itself, including a complete parallel disaggregation in all the observed fragmentation patterns;
- if the impact is close to, but not exactly at, 90°, meridian cracks in the intact material also appear, while a complete top cone pattern is never observed;
- for 0° and 45°, the number of cracks increases with the rise in impact velocity, similar to the behaviour observed

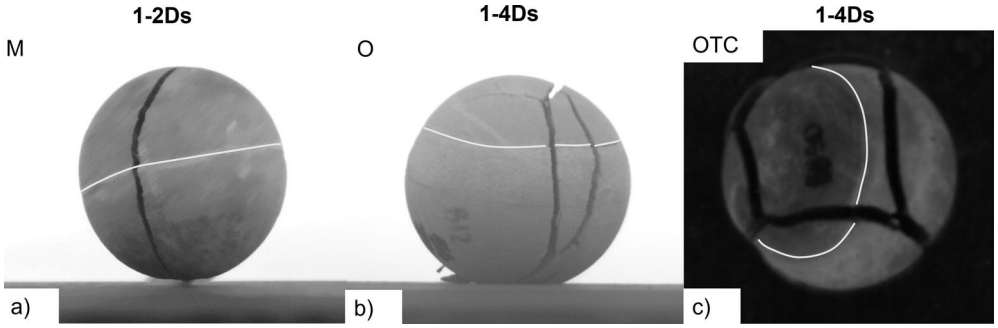

Fig. 7 Examples of the observed fragmentation patterns for all the investigated series when the influence of the discontinuities is negligible. White lines highlight the trace of the discontinuities on the spheres. Pictures with a black background are shot from above, while those with a light background are in front view. The details on the nomenclature of the series are explained in Sect. 2.2

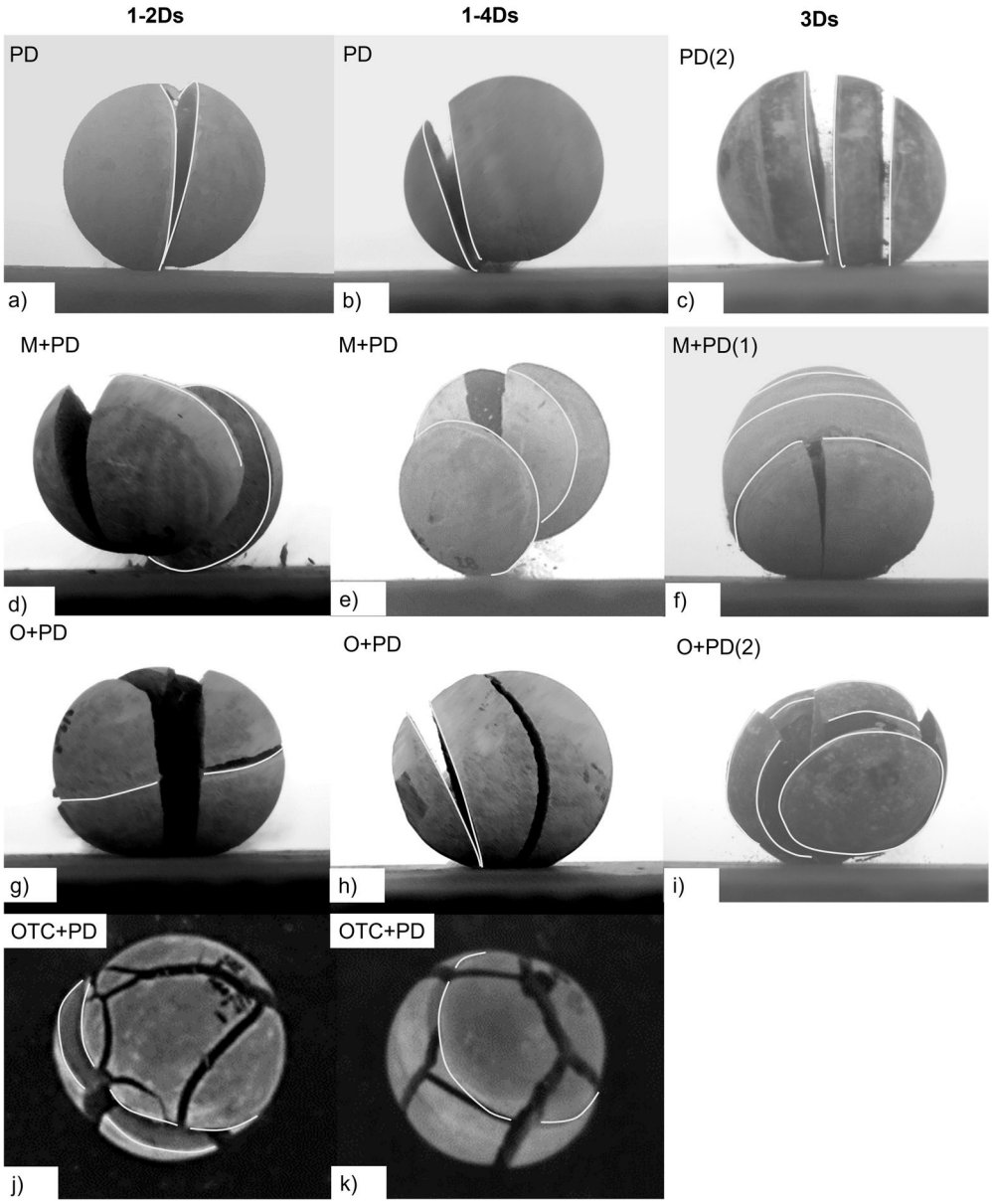

Fig. 8 Examples of the observed fragmentation patterns for all the investigated series when the influence of the discontinuities is not negligible. White lines highlight the trace of the discontinuities on the spheres. Pictures with a black background are shot from above, while those with a light background are in front view. The details on the nomenclature of the series are explained in Sect. 2.2

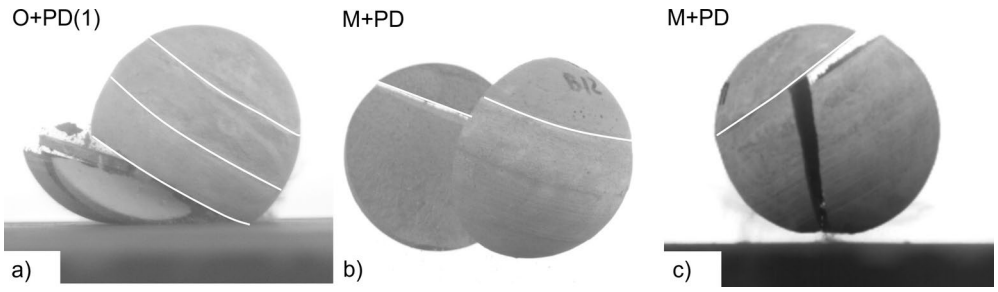

Fig. 9 Front view photos after the impact of: O+PD(1) in the 3Ds series, with a complete PD(1) but incomplete O (**a**), M+PD in the 1–4Ds series, with a complete M but incomplete PD (**b**), and M+PD in the 1–4Ds series with both M and PD incomplete. White lines highlight the trace of the discontinuities on the spheres. The details on the nomenclature of the series are explained in Sect. 2.2

in homogeneous spheres (Arbiter 1969; Wu et al. 2004; Guccione et al. 2023);
- the formation of a top cone occurs exclusively at 0° and 45°, and is associated with high impact energy, specifically $v_i = 10$ m/s, as observed in homogeneous spheres (Guccione et al. 2023).

Although these results pertain to a dynamic load case, they align with the observations of Han et al. (2022) and Xu et al. (2024) for a static load: when the loading axis is normal to the discontinuity, tensile failure occurs exclusively along the loading axis. As the angle between the loading axis and the discontinuity decreases, combined shear-tensile or shear failure modes occur, characterized by shear along the discontinuity. Conversely, when the loading axis is parallel to the discontinuity, tensile failure along the discontinuity is observed.

3.2.2 1–4Ds Series

Considering the 1 4Ds configuration, a trend similar to that observed for 1 2Ds emerges in terms of the percentage of intact samples, particularly for the 0° and 90° impact angle categories. For $\theta = 45°$, the position of the discontinuity relative to the impact point plays a key role: the farther the discontinuity from the impact surface (i.e., 45°t), the higher the percentage of unfragmented samples. An examination of the fracture patterns reveals the significant influence of both the presence and inclination of the discontinuity relative to the slab, as well as the distance and area of the discontinuity plane. Specifically, a unique O and two OTC (without PD) occur at 0° and 10 m/s, while three OTC are observed at 45°t at the same velocity, showing that patterns without PD can occur even at 10 m/s. This differs from the 1 2Ds configuration, in which PD is observed, and highlights the effect of the position of the discontinuity on the crack pattern. Additional observations can be summarised as follows:

- as expected, the number of meridian cracks increases with impact velocity (as in the 1 2Ds configuration), although these cracks often terminate at the discontinuity interface: M+PD failure predominantly occurs at lower velocities, while at higher velocities O+PD or even OTC+PD failures become more prevalent;
- a top cone forms at $v_i = 10$ m/s for nearly all angles, except at 45°b;
- parallel disaggregation occurs at all velocities and is typically the sole fracture mode when the impact occurs directly on the discontinuity plane (i.e., $\theta \approx 60°$, Fig. 6b). Additional cracks may form if the impact is slightly offset. For instance, in the 45°b category, impacts below the discontinuity tend to produce single or multiple meridian cracks;
- the distance between the discontinuity plane and the impact surface significantly affect the fragmentation pattern: for the 45°b case, the smaller bottom part of the sphere completely fragments, with cracks stopping at the discontinuity interface. In contrast, for 45°t, meridian cracks can propagate through the entire sample;

3.2.3 3Ds Series

The percentages reported in Table 4 indicate that the number of discontinuities, i.e. the joint density, significantly affects the proportion of samples that remain intact after impact. For example, at 5 m/s, 58% of the 1–2Ds series (with a single discontinuity) remain intact, compared to just 14% for the 3Ds series. Only a few cases survived the impact. For $v_i = 3$, 4, and 5 m/s, intact samples were observed only in the 'Before 1' impact angle category, and only when $\theta < 30°$. In the single intact sample from the 'On 2' category at 3 m/s, a crack formed along the discontinuity without complete separation. These results align with Han and Yang (2021), confirming that the percentage of intact samples reflects the

Table 4 Percentage of fragmentation pattern types. Percentages should be considered per column, i.e., for equal impact velocity and impact angle category, or for equal velocity only ('Tot.'). For the 3Ds samples, A = Before 1, B = On 1, C = Between 1 &2, D=On 2

1–2Ds															
Velocity	5 m/s			6 m/s			7 m/s			8.5 m/s			10 m/s		
Impact angle cat.	0°	45°	90°	0°	45°	90°	0°	45°	90°	0°	45°	90°			
Intact	100	64	10	83	56	–	40	14	–	–	–	-	-	-	–
M	–	–	–	–	–	–	30	3	–	–	–	–	–	–	–
M+PD	–	6	20	–	22	29	–	34	54	–	–	50	–	–	78
O	–	–	–	8	–	–	10	–	–	–	–	–	–	–	–
O+PD	–	6	–	8	22	7	20	48	15	100	100	50	60	67	11
OTC+PD	–	–	–	–	–	–	–	–	–	–	–	–	40	33	–
PD	–	24	70	–	–	64	–	–	31	–	–	–	–	–	11
Tot. Intact	58			47			15			–			–		
Tot. M	–			–			8			–			–		
Tot. M +PD	8			19			33			7			35		
Tot. O	–			2			2			–			–		
Tot. O+PD	4			15			35			93			40		
Tot. OTC+PD	–			–			–			–			20		
Tot. PD	30			17			8			–			5		

1–4Ds												
Velocity	6 m/s				7 m/s				10 m/s			
Impact angle cat.	0°	45*t*°	90°	45*b*°	0°	45*t*°	90°	45*b*°	0°	45*t*°	90°	45*b*°
Intact	100	71	–	–	33	45	–	–	–	–	–	–
M+PD	–	14	33	67	33	27	60	–	–	–	–	20
O	–	–	–	–	–	–	–	–	25	–	–	–
O+PD	–	14	50	–	33	27	20	100	25	33	40	80
OTC	–	–	–	–	–	–	–	–	50	25	–	–
OTC+PD	–	–	–	–	–	–	–	–	–	42	60	–
PD	–	–	17	33	–	–	20	–	–	–	–	–
Tot. Intact	42				24				–			
Tot. M+PD	29				28				4			
Tot. O	–				–				4			
Tot. O+PD	17				44				42			

Table 4 (continued)

1–4Ds

Velocity	6 m/s				7 m/s				10 m/s			
Impact angle cat.	0°	45*t*°	90°	45*b*°	0°	45*t*°	90°	45*b*°	0°	45*t*°	90°	45*b*°
Tot. OTC	–				–				19			
Tot. OTC+PD	–				–				31			
Tot. PD	13				4				–			

3Ds

Velocity	3 m/s				4 m/s				5 m/s				6 m/s				7 m/s			
Impact angle cat.	A	B	C	D	A	B	C	D	A	B	C	D	A	B	C	D	A	B	C	D
Intact	50	–	–	9	50	–	–	–	23	–	–	–	–	–	–	–	–	–	–	–
M	–	–	–	–	–	–	–	–	3	–	–	–	–	–	–	–	–	–	–	–
M+PD1	11	–	–	–	17	–	–	–	17	–	–	–	–	–	–	–	10	–	–	–
M+PD2	–	–	–	–	–	–	–	–	–	50	82	–	–	–	63	–	–	100	100	–
M+PD3	–	–	–	–	–	–	–	–	–	–	–	–	–	–	13	–	–	–	–	–
O+PD1	–	–	–	–	4	–	–	–	53	–	–	–	100	–	–	–	80	–	–	–
O+PD2	–	–	–	–	–	–	–	–	–	–	–	–	–	–	25	–	–	–	–	–
PD1	38	–	60	82	29	100	20	63	3	50	–	50	–	–	–	33	10	–	–	–
PD2	–	–	20	9	–	–	60	25	–	–	9	50	–	–	–	67	–	–	–	67
PD3	–	–	20	–	–	–	20	13	–	–	9	–	–	100	–	–	–	–	–	33
Tot. Intact	33				30				14				–				–			
Tot. M	–				–				2				–				–			
Tot. M+PD1	7				10				10				–				5			
Tot. M+PD2	–				–				22				23				38			
Tot. M+PD3	–				–				–				5				–			
Tot. O+PD1	–				2				31				45				38			
Tot. O+PD2	–				–				–				9				–			
Tot. PD1	52				41				12				5				5			
Tot. PD2	5				12				8				9				10			
Tot. PD3	2				5				2				5				5			

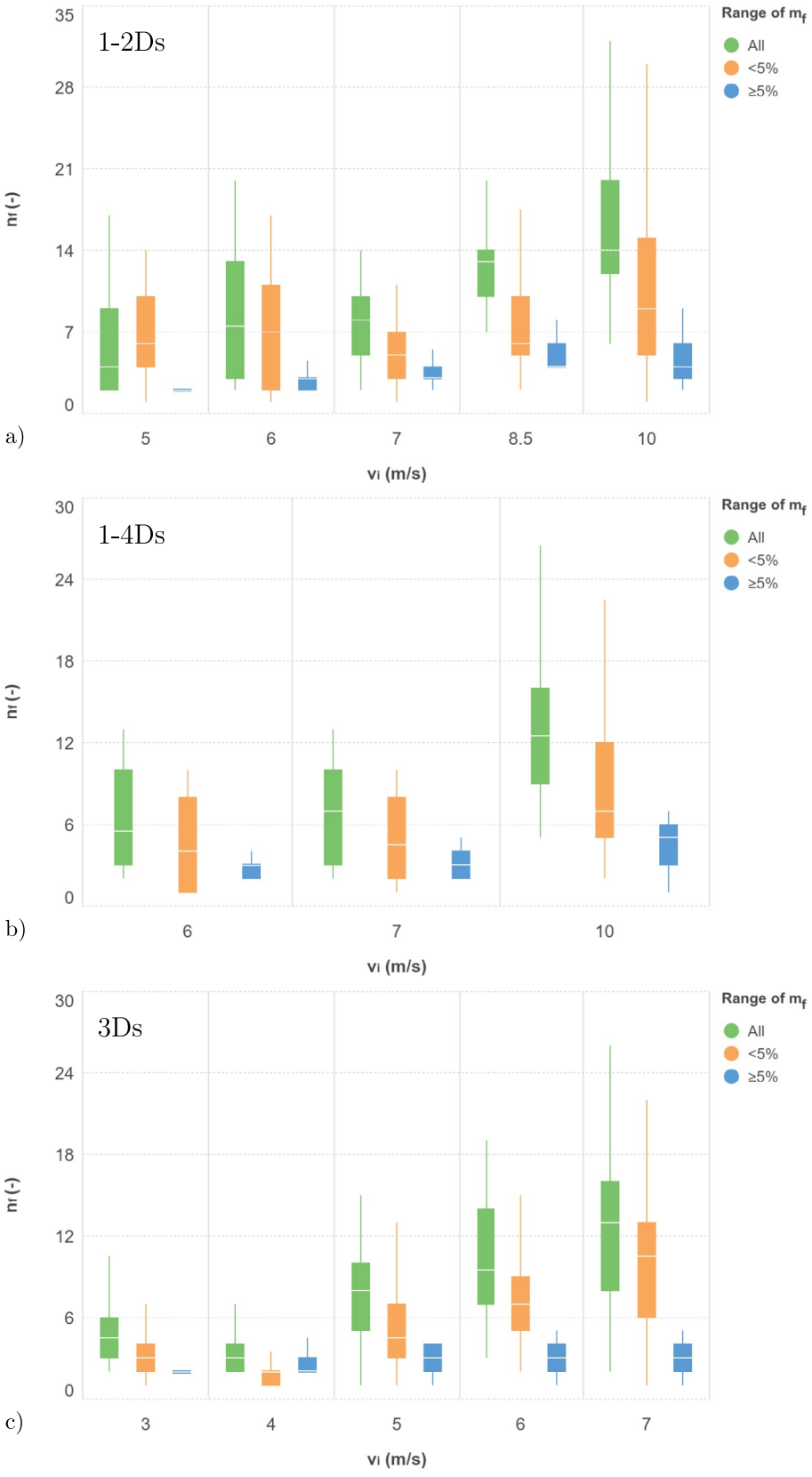

Fig. 10 Boxplots of the number of fragments n_f for each impact velocity and each series (**a**–**c**), considering all the fragments, those with mass $m_f < 5\%$ and $m_f \geq 5\%$ of the mass of the intact sample

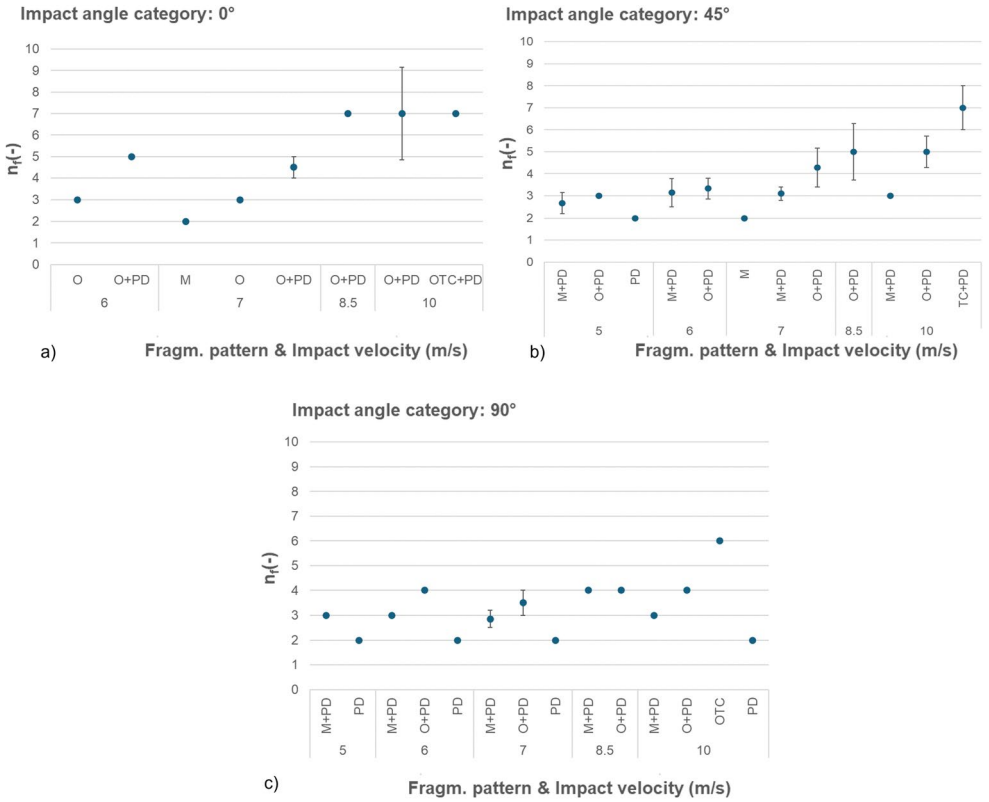

Fig. 11 Average number of fragments n_f and standard deviation for each impact angle category (**a** 0°, **b** 45°, **c** 90°) as a function of impact velocity v_i and fragmentation pattern, for 1–2Ds series

decreasing tensile resistance as joint density increases. Additional observations include:

- at lower velocities (3 and 4 m/s), pure parallel disaggregation (PD) occurs across all impact angle categories, typically along one or more discontinuities. As velocity increases, PD alone becomes less frequent, mainly occurring when discontinuities align with or are parallel to the loading axis;
- in the 'Before 1' category, PD along a single discontinuity (PD1) is mainly observed at lower velocities when $\theta > 30°$. At higher velocities, fragmentation transitions: several meridian cracks form in the lower part and terminate at the first encountered discontinuity (similar to the 1–4Ds series). This suggests that also the spatial arrangement of the discontinuities, specifically, the distance between the impact plane and the nearest discontinuity, plays a role in the resulting failure pattern;
- in the 'Between 1 &2' category, M+PD2 is the most common failure mode for $v_i \geq 5$ m/s, with a meridian crack forming between discontinuities at 1/4 and 1/2 of the sphere, and PD along both. At lower velocities, only parallel disaggregation occurs;
- no top cone formation is observed, although the 10 m/s case was not investigated for this series.

3.3 Quantitative Fragments Distribution Analysis

In this section, for each series, the evolution of the number of fragments as a function of impact velocities v_i is first discussed. Then, the cumulative number of fragments is presented as a function of the fragment mass. All the fragments with masses $m_f \geq 0.2$ g ($\approx 0.02\%$ of the initial mass m_i) were recorded and subdivided in small ($m_f < 5\%$ of the initial mass) and large fragments ($m_f \geq 5\%$ of the initial mass). This size threshold was defined accordingly with (Guccione et al. 2023).

3.3.1 1–2Ds Series

The boxplot in Fig. 10a summarises the number of fragments n_f per test generated upon impact, grouped according to the impact velocity. The bottom and top of each box represent the 25th and 75th percentiles of the sample, i.e., the first and third quartiles, respectively. The white line indicates the median, i.e., the 50th percentile of the distribution. For

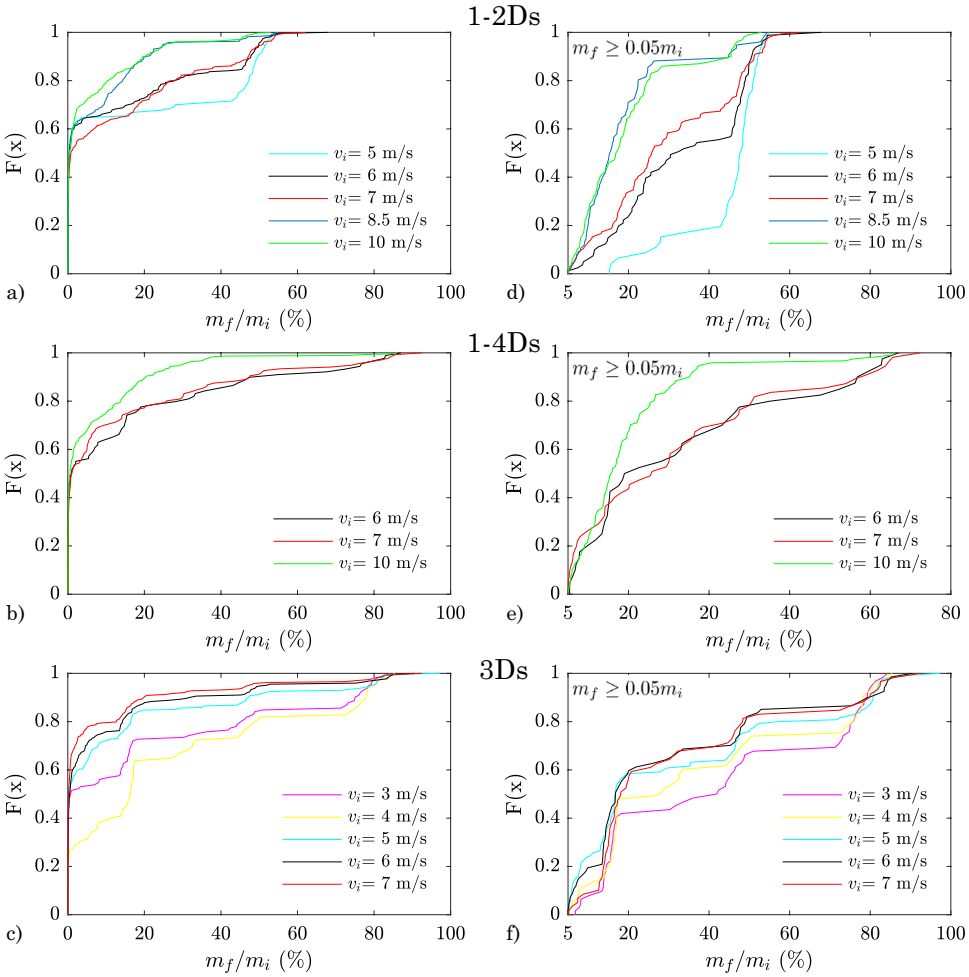

Fig. 12 Empirical cumulative distribution function of all the fragment masses for the 1–2Ds (**a**), 1–4Ds (**b**), and 3Ds (**c**) series, and of fragment masses above 5% of the initial mass for the 1–2Ds (**d**), 1–4Ds (**e**), and 3Ds (**f**) series

each velocity, statistics are reported for (i) all the recorded fragments, (ii) small fragments, (iii) and large fragments.

As expected, an increase in impact velocity generally corresponds to an increase in the number of fragments for all the analysed classes. A large number of small fragments, up to 30 fragments per test, is observed for 10 m/s.

Considering fragments with $m_f \geq 5\%$ of the initial mass, only, Fig. 11 reports the average number of fragments n_f and its standard deviation for each impact angle category as a function of impact velocity v_i and fragmentation pattern. As a general trend, for all the impact angle categories, the average number of fragments increases as function of the number of cracks associated to the fragmentation pattern, with a minimum of 2 fragments for M or PD, a typical number of 3 fragments for M+PD, to a maximum of 7 for OTC+PD case.

Figures 12a and d present the empirical cumulative distribution function $F(x)$ for all fragment masses and for fragments with $m_f \geq 5\%$ of the initial mass m_i, respectively. As already observed, an increase of the impact velocity corresponds to an increase of the number of fine fragments, which generally constitute a percentile greater than 0.4. A low variability is observed for v_i between 8.5 and 10 m/s (the curves can be superimposed) with finer fragments compared to slower velocities. The maximum fragment size was estimated to be approximately half the initial mass ($\approx$ 500 g). The presence of a plateau at $F(x) = 0.95$ starting from $m_f \approx 0.26m_i$ for $v_i \geq 8.5$ m/s indicates the occurrence of a significant number of secondary cracks.

3.3.2 1–4Ds Series

Similarly to the 1–2Ds series, Fig. 10b summarises the number of fragments n_f generated upon impact, grouped for impact velocity and fragment mass, while Fig. 13 reports the average number of fragments n_f (and its standard deviation). As for the 1–2Ds series, an increase in impact velocity corresponds to an increase in the number of fragments, with a large number of small fragments (up to 27 fragments at 10 m/s). Considering the impact angle category, the average number of fragments spans from 2 to 6. For both 0° and 45t°, the fragmentation pattern M+PD often displays incomplete cracks, resulting in just two fragments. In the 45b° impact angle category, the smaller portion identified

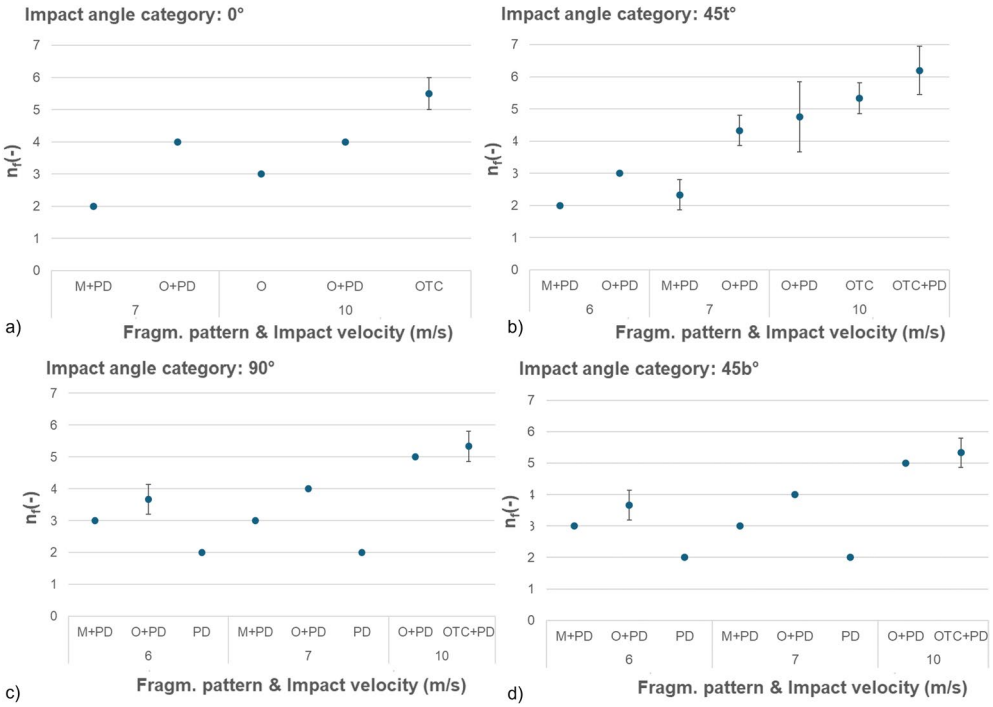

Fig. 13 Average number of fragments n_f and standard deviation for each impact angle category (**a** 0°, **b**: 45*t*°, **c**: 90°, **d**: 45*b*°) as a function of impact velocity v_i and fragmentation pattern, for 1–4Ds series

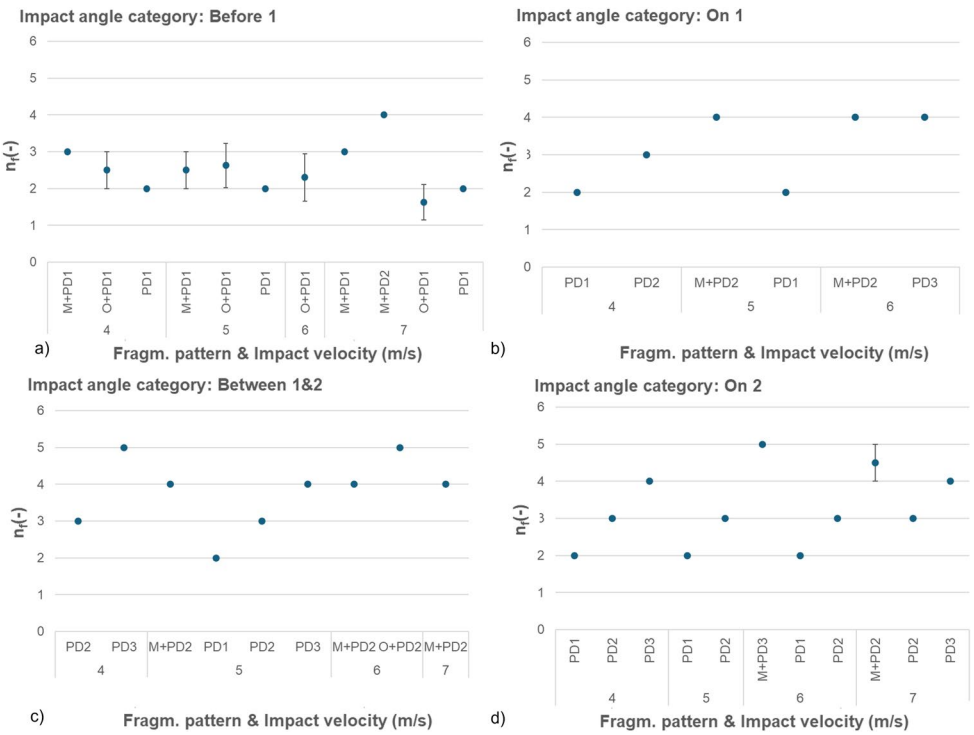

Fig. 14 Average number of fragments n_f and standard deviation for each impact angle category (**a**: Before 1, **b**: On 1, **c**: Between 1 & 2, **d**: On 2) as a function of impact velocity v_i and fragmentation pattern, for 3Ds series

by the discontinuity tends to separate into several fragments, some of which classified as small ($m_f \leq 0.05m_i$).

Considering the empirical cumulative distribution function of fragment mass (Fig. 12b, e), at $v_i = 10$ m/s, 95% of the fragments have a mass $m_f \leq 0.4m_i$. No plateaux are observed at lower impact velocities, suggesting the existence of velocity (or energy) thresholds for transitioning between fragmentation regimes. The maximum fragment mass is approximately $0.8m_i$, corresponding to the portion identified by the discontinuity. Similar to the 1–2Ds case, a significant discrepancy is noted at $v_i = 10$ m/s compared to lower velocities, which curves can be superimposed.

3.3.3 3Ds Series

Similar to the other series, Fig. 10c summarizes the number of fragments n_f generated upon impact for the 3Ds series, while Fig. 14 presents the average number of fragments. Compared to the other series, the 3Ds series shows an increase in the average number of fragments at $v_i = 6$ and 7 m/s, emphasizing the impact of the number of discontinuities on the fragmentation process. The same median values are observed for v_i =3 and 4 m/s, equal to 3 fragments.

Figure 14 illustrates an average number of fragments ranging between 2 and 5, with higher values observed for the 'Between 1 &2' and 'On 2' impact angle categories. For impact angle categories other than 'Before 1', an equal number of fragments is noted for identical fracture patterns, regardless of the impact velocity. In the 'Before 1' scenario, however, incomplete cracks may occur, accompanied by severe fragmentation of the bottom part into small fragments.

The cumulative distribution of fragment mass (Fig. 12c, f) underscores the impact of discontinuities configurations on fragment mass. For all impact velocities, a stepped curve is observed, corresponding approximately to the portions of the sample divided by the discontinuities at 1/4, 1/2, and 3/4 of the sample, i.e., $m_f \approx 0.2, 0.5$, and 0.8 of the initial mass, respectively. This results in a fragment size distribution that deviates from the generally observed power law (Arbiter 1969; Lanfranconi et al. 2023).

3.4 Fragments Trajectories

A total of 119 drop tests were tracked: 46 tests for the 1–2Ds series, 27 for the 1–4Ds, and 46 for the 3D. The rationale behind the selected tests was to ensure a statistically representative number for each series and impact velocity. For each fracture pattern and impact angle category, a minimum of three tests were tracked under identical impact velocities, v_i. Additionally, the images of excluded tests were examined to ensure no particular cases were overlooked and that the fragment sizes and trajectories were consistent with those observed in tests with similar impact characteristics. For each test, the trajectories of fragments with known masses were analysed, and the post-impact velocity vector, v_f, was estimated by considering its components in the ξ, η, and z directions (see Sect. 2.1 for details), i.e., v_ξ, v_η, and v_z, respectively. It is worth recalling that the ξ-axis represents the projection onto the impact plane of the vector normal to the discontinuity plane. To express the velocity vector in the global x y z reference system, in the context of rockfall propagation analysis, let ϕ denote the positive anti-clockwise angle between the projection of the ξ-axis and the x-axis. The velocity components then transform as follows:

$$v_x = \cos\phi v_\xi - \sin\phi v_\eta \tag{2}$$

$$v_y = \sin\phi v_\xi + \cos\phi v_\eta, \tag{3}$$

while v_z remains unchanged. As reported in Sect. 2.1, the planar angle β (measured clockwise from the η-axis to the velocity vector) was used to assess the distribution of velocity directions on the ξ η plane, while the angle α, defined between the vertical and the ξ η velocity components, was used to quantify the vertical projection of the fragment.

The results were initially grouped based on v_i, and subsequently organized according to: (i) impact angle category, (ii) fragment sizes, and (iii) fragmentation patterns.

3.4.1 1–2Ds Series

Figure 15 shows the velocity vectors in the ξ η plane for all analysed fragments, while Fig. 16 presents their projections onto the ξ z and η z planes.

At $v_i = 5$ m/s, fragmentation mainly produces fragments with v_z up to 1 m/s (Table 5). In the ξ η plane, fragments align along the ξ-axis ($\beta \approx 90°$ and 270° in Fig. 17), regardless of mass. For $\theta = 90°$, fragments are ejected in both $\pm\xi$ directions, while at $\theta = 45°$, most fragments move in the $+\xi$ direction, with the top half sliding along the discontinuity and then on the slab (Fig. 18a1, a2). Occasionally, the upper part is projected vertically.

At $v_i = 6$ m/s, a similar pattern is observed, with additional fragmentation at $\theta = 0°$ and slightly higher v_ξ values (up to 1.7 m/s). Fragments moving in the $-\xi$ direction typically result from parallel disaggregation, especially at $\theta = 90°$. A single test shows significant deviation from the ξ -axis, involving small fragments (~75 g, 0.7% of the initial mass) in an O+PD scenario.

At higher velocities, fragments increasingly deviate from the ξ-axis: up to 30° at 7 m/s, 45° at 8.5 m/s, and become

Table 5 Maximum and minimum (maximum in negative direction) values of the velocity components observed in each series for each impact velocity v_i

1–2Ds										
v_i	5 m/s		6 m/s		7 m/s		8.5 m/s		10 m/s	
axis	≥0	<0	≥0	<0	≥0	<0	≥0	<0	≥0	<0
v_ξ (m/s)	1.53	−1.12	1.88	−1.14	2.28	−1.62	3.07	−1.66	3.03	−2.32
v_η (m/s)	0.21	−0.20	1.01	−0.61	1.30	−1.17	2.25	−1.74	2.21	−2.50
v_z (m/s)	1.14	−0.20	1.00	−0.03	1.57	−0.01	0.89	−0.04	1.92	−0.94

1–4Ds						
v_i	6 m/s		7 m/s		10 m/s	
axis	≥0	<0	≥0	<0	≥0	<0
v_ξ (m/s)	2.32	−0.71	2.04	−1.03	3.40	−2.67
v_η (m/s)	0.62	−0.52	0.70	−0.67	2.46	−3.19
v_z (m/s)	1.56	−0.79	1.21	−0.55	2.44	−1.01

3Ds										
v_i	3 m/s		4 m/s		5 m/s		6 m/s		7 m/s	
axis	≥0	<0	≥0	<0	≥0	<0	≥0	<0	≥0	<0
v_ξ (m/s)	0.54	−0.70	1.54	−0.89	1.53	−1.13	1.93	−1.95	2.44	−2.27
v_η (m/s)	0.10	−0.12	0.42	−0.20	0.69	−0.67	1.16	−1.47	0.79	−1.38
v_z (m/s)	0.96	/	1.01	−0.45	0.90	−0.86	2.37	−0.66	1.21	−0.54

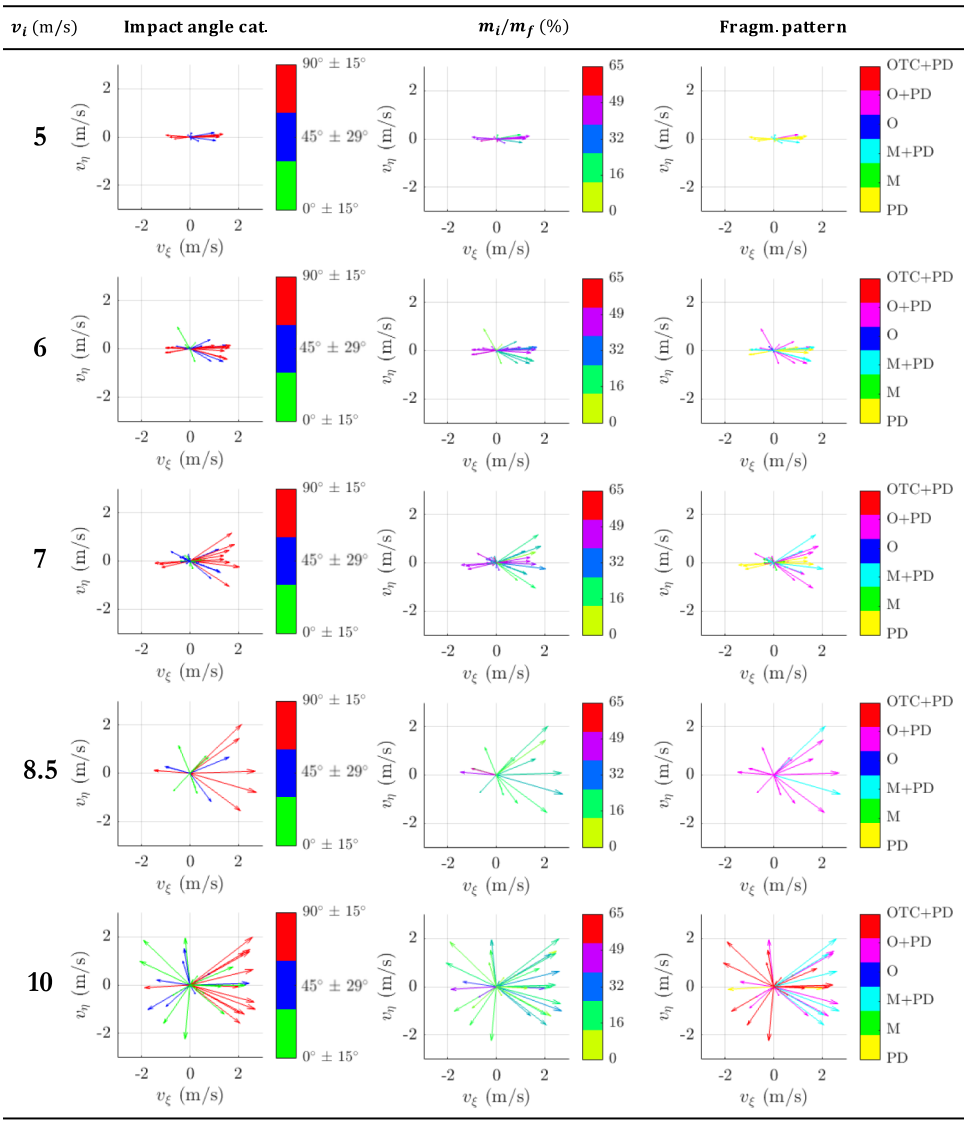

Fig. 15 Post-impact velocity vectors of the fragments for the 1–2Ds series, for all the velocities, in the $\xi - \eta$ plane, subdivided according to impact angle category (left column), mass of the fragments (middle column), and type of fracture (right column). Each row corresponds to an impact velocity v_i

widely dispersed at 10 m/s. This trend is less evident at $\theta = 90°$. Notably, fragments with greater deviation tend to be smaller (up to 25% of the original mass), while the largest fragments, typically from PD, remain aligned with the ξ-axis. As v_i increases, both $|v_\xi|$ and $|v_\eta|$ grow, while v_z remains largely unaffected by impact angle or velocity. Consequently, the throw angle α decreases beyond 7 m/s. The highest α values occur at $\theta = 45°$ and 7 m/s in M+PD cases, where the impacted half rebounds vertically and the other half slides or rolls, as seen at 5 m/s (Fig. 18a1, a2). Conversely, low α values are typical for $\theta = 90°$, where horizontal velocities dominate.

To summarize, increasing impact velocity leads to a greater number of fragments, higher velocity magnitudes, and wider directional dispersion within the impact plane. Vertically, negative v_z components become more frequent. Larger fragments, typically resulting from parallel disaggregation, tend to move along the impact plane with low throw angles, aligned with the normal to the discontinuity plane. The minimal dispersion observed at low impact velocities is likely due to fewer cracks forming in the intact rock and more along pre-existing discontinuities. From a trajectory modelling perspective, although this suggests that discontinuities may reduce the likelihood of wide dispersion, at least for low velocities, the unknown orientation of these planes in natural slopes limits deterministic modelling. Nevertheless this confirm that the commonly assumed fixed cone of dispersion (Matas et al. 2020; Frattini et al. 2012; Lanfranconi et al. 2023) may not apply. Field and real-event

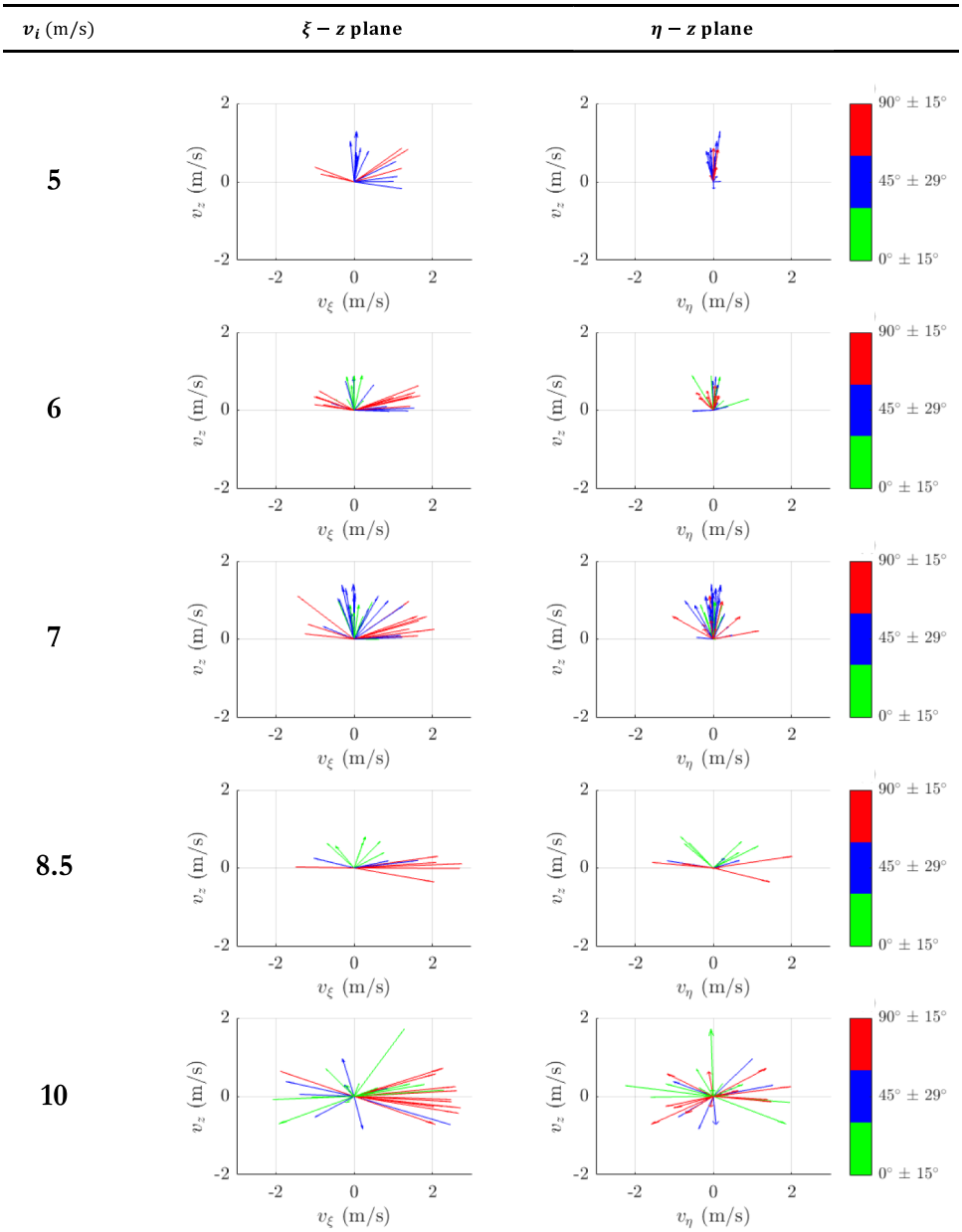

Fig. 16 Post-impact velocity vectors of the fragments for the 1–2Ds series, for all the velocities, in the $\xi - z$ and $\eta - z$ planes subdivided according to impact angle category. Each row corresponds to an impact velocity v_i

data (Gili et al. 2018, 2022; Lanfranconi et al. 2024) report deviations from the pre-impact trajectory ranging from 25° to 145° (mode: 75°), supporting the need for more flexible, probabilistic trajectory models. Thus, the observed trend of increasing dispersion with impact velocity could be effectively integrated into such models to enhance realism.

3.4.2 1–4Ds Series

Similarly to the 1 2Ds series, Figs. 19 and 20 show the velocity vectors in the $\xi\,\eta$, $\xi\,z$, and $\eta\,z$ planes, while Fig. 21 reports the β and α angles for all fragments.

At $v_i = 6$ m/s, fragments predominantly move along the ξ direction (up to 2.3 m/s), except in one 90° impact case where a meridian crack causes significant deviation

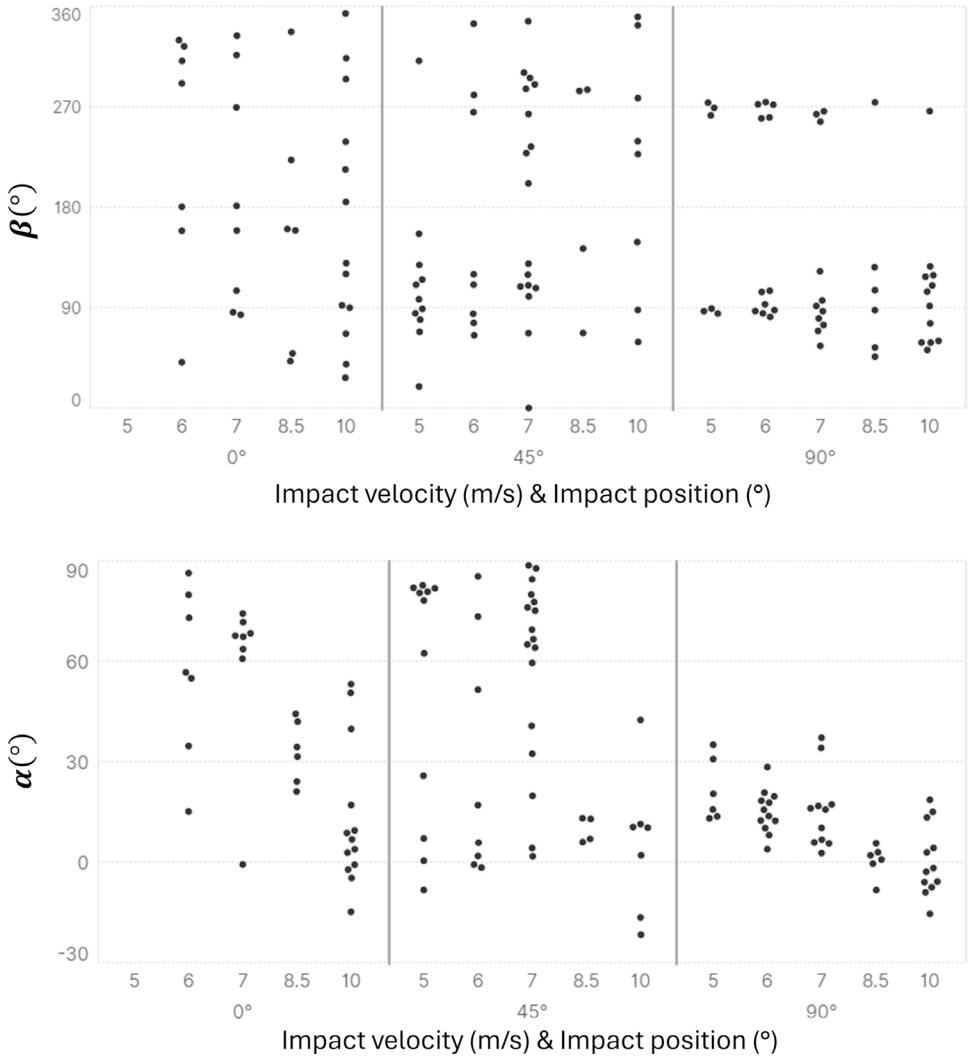

Fig. 17 β and α angles for all fragments as a function of impact angle category and impact velocity for the 1–2Ds series

(Fig. 18b). Negative v_z values are observed in 45b° impact cases with $\theta \approx 65°$ 70°, where the smaller portion detaches and falls due to gravity (Fig. 18c). When $\theta \leq 50°$, fragments move along the slab with velocities confined to the $\xi\,\eta$ plane (Fig. 18d). In the 45t° case, fragments are ejected vertically ($\alpha \approx 80°$), a behaviour that has not observed at other velocities.

For $v_i = 6$ and 7 m/s, M+PD and O+PD fragmentation types often produce fragments with mirrored trajectories relative to the ξ-axis, with similar magnitudes (Fig. 18b). This mirroring occurs in both positive and negative ξ directions depending on the impact angle. The largest fragments ($m_f \geq 50\%$) tend to move along the negative ξ direction. At $v_i = 10$ m/s, fragment trajectories become highly dispersed across all directions, with increased velocity magnitudes (Table 5).

As in the 1 2Ds series, increasing impact velocity leads to more fragments and wider dispersion in the impact plane. For $v_i \leq 7$ m/s, large fragments move with low throw angles along the discontinuity normal, while smaller fragments are often ejected in mirrored directions with significant v_z components. The velocity magnitude increases with impact velocity. From a propagation perspective, the unknown orientation of discontinuities relative to the slope makes trajectory prediction difficult.

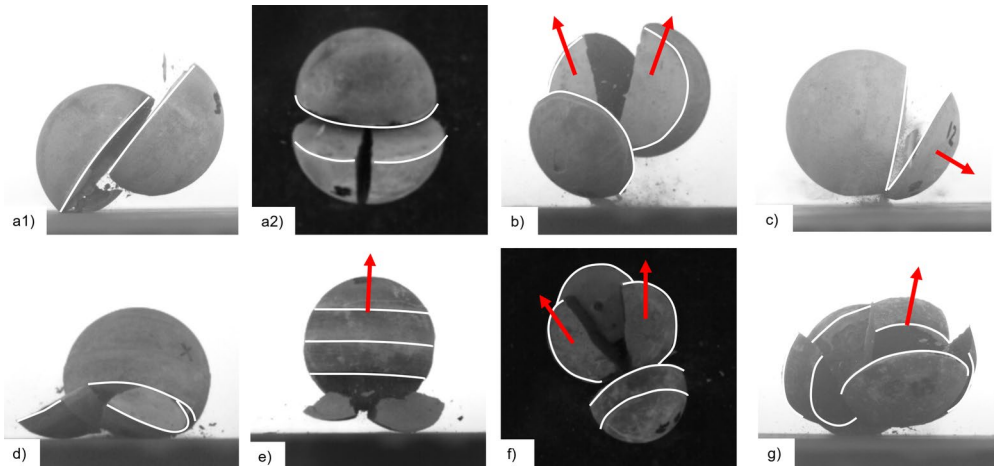

Fig. 18 Front (**a1**) and top (**a2**) view of a M+PD case for a v_i = 5 m/s, 45° impact angle category for the 1–2Ds series; front view of a M+PD case for a v_i =6 m/s, 90° impact angle category for the 1–4Ds series (**b**); front view of a M+PD case for a v_i =6 m/s, 45°*b* impact angle category for the 1–4Ds series (**c**); front view of a M+PD case for a v_i =6 m/s, 45°*b* impact angle category for the 1–4Ds series (**d**); front view of a O+PD1 case for a v_i =7 m/s, 'Between 1' impact angle category for the 3Ds series (**e**); top view of a M+PD2 case for a v_i =5 m/s, Between 1 &2' impact angle category for the 3Ds series (**f**); front view of a O+PD2 case for a v_i =6 m/s, 'Between 1 &2' impact angle category for the 3Ds series (**g**); White lines highlight the trace of the discontinuities on the spheres, while red arrows qualitatively represent the velocity vector of some fragments

3.4.3 3Ds Series

Figures 22 and 23 show the velocity vectors in the $\xi\,\eta$, $\xi\,z$, and $\eta\,z$ planes for the 3Ds series, while Fig. 24 reports the β and α angles.

At $v_i = 3$ and 4 m/s, fragment trajectories are mainly aligned with the ξ-axis ($\beta \approx 90°$ and 270°), except for one 4 m/s case ('Before 1' category) where the bottom part fragments (M or O type) and the top rebounds ($\alpha \approx 70°$), with lateral ejection along η (Fig. 18e). Negative v_z values appear only from $v_i = 4$ m/s onward.

For $v_i \geq 5$ m/s, especially in the 'Between 1 &2' category with M+PD2 or M+PD3 patterns, velocity vectors spread fan-like along the positive ξ direction ($50° \leq \beta \leq 140°$ for $v_i = 5$ m/s, and up to approximately $40° \leq \beta \leq 130°$ for higher impact velocities), while remaining more concentrated on the negative side (Fig. 24). In these cases, the impacted portion between two discontinuities breaks into smaller fragments ($m_f \leq 25\%$) moving in opposite η directions, while larger fragments from parallel disaggregation move oppositely in the $\xi\,z$ plane (Fig. 18f).

Across all velocities, more fragments tend to move in the positive ξ direction. Maximum v_z values are generally around 1 m/s, with a single case reaching 2.37 m/s at 6 m/s (O+PD2, Fig. 18g), where meridian cracks split the impacted part into three fragments. In 'On 1' impacts, two or three fragments form: one moves vertically ($\alpha \geq 60°$), the others along ξ with low vertical components ($-20° \leq \alpha \leq 10°$). Velocity components in the $\xi\,\eta$ plane remain similar across all cases.

To summarize, fragment trajectories in the 3Ds series predominantly align with the discontinuities normal, with greater dispersion along the positive ξ direction. Angular dispersion increases with velocity, reaching 40° 50° for $v_i \geq 5$ m/s. Vertical velocity components show no clear trend with velocity. While fragmentation patterns and directions are recurrent, their prediction remains difficult due to the unknown orientation of discontinuities relative to the impact plane.

3.4.4 Restitution Coefficients and Concluding Remarks

Considering all motion types, bouncing, rolling, and sliding, the first dominates across all series: 75% in 1 2Ds, 73% in 3Ds, and 77% in 1 4Ds. Sliding and rolling account for 13 20%, while 3 12% of fragments remain stationary. In the 1 4Ds and 3Ds series, fragments impacted at $\theta \leq 50°$ or in the 'Before 1' category moved exclusively along the slab and were not tracked. In contrast, the 1 2Ds series shows mixed behaviour, with sliding observed at $v_i = 5$ m/s and $\theta \approx 70°$, where one half bounces and the other slides.

From a trajectory perspective, the predominance of bouncing (73 77%) underscores its importance in rockfall dynamics, especially on steep, hard surfaces. While sliding

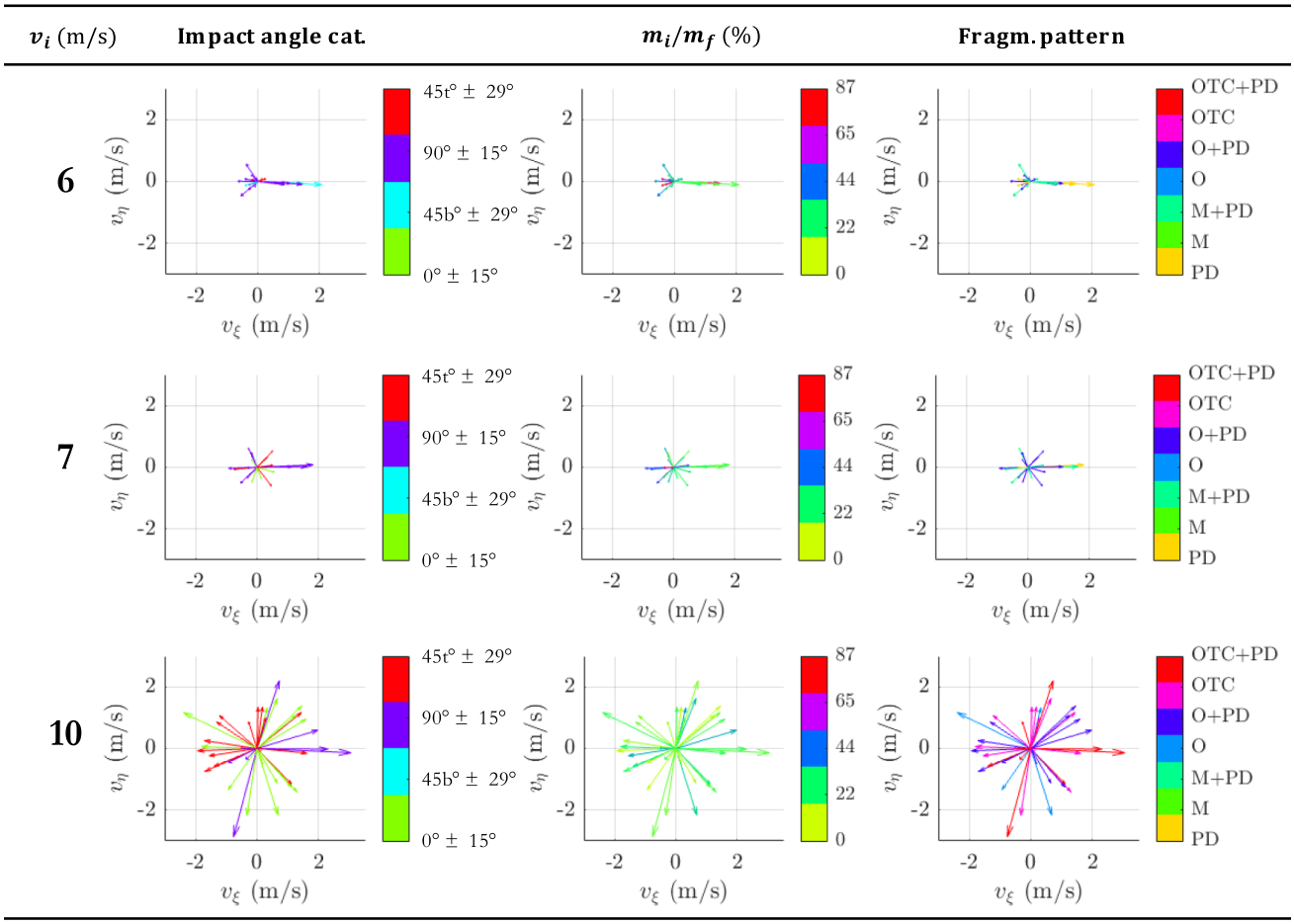

Fig. 19 Post-impact velocity vectors of the fragments for the 1–4Ds series, for all the velocities, in the $\xi - \eta$ plane, subdivided according to impact angle category (left column), mass of the fragments (middle column), and type of fracture (right column). Each row corresponds to an impact velocity v_i

and rolling are relevant for understanding runout and directional stability on continuous slopes, bouncing fragments exhibit more energetic and complex trajectories, higher velocities, greater jump heights, and more variable impact directions, critical for designing effective mitigation measures such as barriers. Image analysis shows that sliding and rolling fragments do not display greater directional dispersion than bouncing ones, supporting the focus on bouncing as the most variable and energetically significant motion type under the tested conditions.

Focusing on bouncing fragments, Fig. 25 shows the coefficient of restitution ($|v_f|/|v_i|$) versus normalized fragment mass (m_f/m_i). Fragment size is influenced by discontinuity configuration, as also noted in Sect. 3.3: in 1 2Ds, fragments rarely exceed 50% of the initial mass, while in 1 4Ds and 3Ds, larger fragments (up to 90%) occur, especially at lower velocities. Across all series, $|v_f|/|v_i|$ is largely independent of impact velocity and generally lower than 0.4, with a maximum of 0.46 in the 3Ds series. Notable clusters related to impact angles emerge across all series. In the 1 2Ds case, higher impact angles θ correspond to higher $\frac{|v_f|}{|v_i|}$ ratios. This trend is less evident in the 1 4Ds series and not observed in the 3Ds series, where the lowest values are associated with the 'Before 1' impact type. For other impact angle categories in the 3Ds series, the values of the ratio are more evenly distributed in the 0.1 0.4 range. Compared to homogeneous spheres (Guccione et al. 2023), which showed $|v_f|/|v_i|$ between 0.18 0.30, the present study reports higher average values (0.35), likely due to the lower energy required to fracture pre-discontinuous samples.

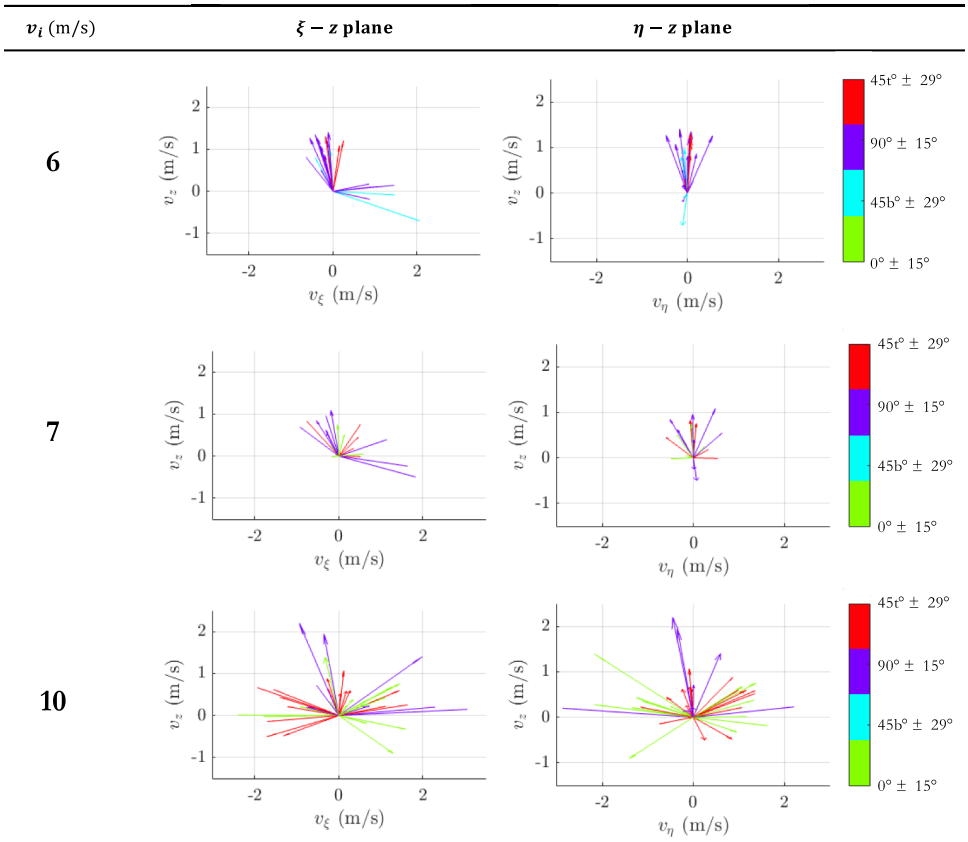

Fig. 20 Post-impact velocity vectors of the fragments for the 1–4Ds series, for all the velocities, in the $\xi - z$ and $\eta - z$ planes subdivided according to impact angle category. Each row corresponds to an impact velocity v_i

The right column of Fig. 25 shows the normal restitution coefficient ($|v_z|/|v_i|$) versus m_f/m_i. Values remain below 0.3 and show no clear dependence on impact angle. A positive correlation between v_z and θ is not evident, though the lowest values occur at $\theta = 0°$ in 1 4Ds. Unlike Guccione et al. (2023), who found a negative correlation between v_i and α in homogeneous samples, the present results highlight the role of discontinuity configuration in fragment ejection. These findings challenge the assumption of uniform post-fragmentation velocities (Matas et al. 2020).

Figure 26 presents the ratio of the post-impact kinetic energy of all bouncing fragments to the initial impact kinetic energy, scaled by the tracked mass. In the 1 2Ds series, this ratio is highest when the discontinuity is normal to the impact surface. While the absolute post-impact energy varies with fragment mass and velocity, the ratio $\frac{E_{out}}{E_i}\frac{m_i}{\Sigma m_f}$ appears largely unaffected by v_i, suggesting that energy dissipation is primarily governed by the inclination of the discontinuity plane relative to the slab. More fragments correspond to lower post-impact energy, consistent with energy loss through fragmentation. In 1 4Ds, higher v_i increases post-impact energy, while fragment count has little effect. In 3Ds, energy remains stable across velocities, with fragment count typically limited to two or three. These results emphasize that a central discontinuity maximizes fracture surface and energy dissipation. Compared to homogeneous spheres (Guccione et al. 2023), which yield fewer bouncing fragments, the 1 2Ds and 1 4Ds series show greater energy loss due to more extensive fragmentation.

4 Conclusions

Fragmentation during rockfall events significantly influences the size, number, and trajectories of falling blocks, yet the role of pre-existing discontinuities in this process remains poorly understood. This study investigated the fragmentation of brittle mortar spheres with artificially embedded discontinuities via controlled drop tests. Using the University of Newcastle's fragmentation cell and high-speed imaging, we analysed failure mechanisms, fragmentation patterns, and fragment trajectories. The selected configurations, i.e. central (1–2Ds), offset (1–4Ds), and multiple parallel discontinuities (3Ds), were designed to assess the influence

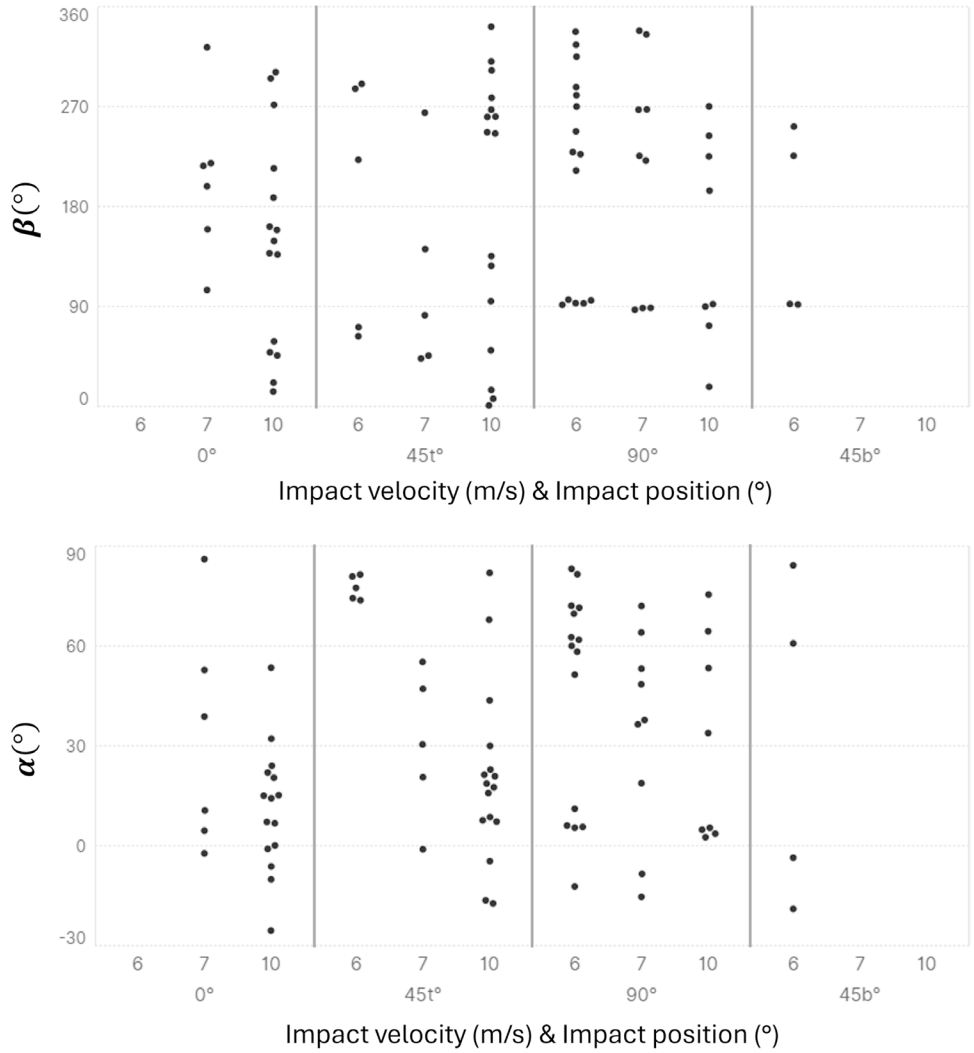

Fig. 21 β and α angles for all fragments as a function of impact angle category and impact velocity for the 1–4Ds series

of discontinuity presence, joint density, and persistence on fragmentation dynamics. Additionally, the role of impact conditions, specifically impact velocity and the inclination of the discontinuity plane relative to the impact surface, was found to be fundamental in controlling fragmentation outcomes.

The results highlight how both the geometry of internal discontinuities and the impact conditions influence fragmentation mechanisms, fragment size distributions, and post-impact trajectories, and the key findings include:

- fragmentation is limited at low impact velocities (v_i) and when the impact direction is normal to the discontinuity(ies) plane(s). As v_i increases, the number of primary and secondary cracks rises, with top-cone patterns observed only at 10 m/s;
- failure modes depend on the inclination of the discontinuity plane relative to the impact surface. Tensile failure in the intact material dominates when the plane is nearly parallel to the slab, while inclined configurations lead to tensile-shear or shear failure. When the loading axis aligns with the discontinuity, tensile-like failure occurs along the joint;
- fragment number (typically 2 7 for $m_f > 5\%\ m_i$) and size are influenced by both impact velocity and discontinuity configuration. In 1–2Ds and 1–4Ds, higher v_i increases fragmentation. In 3Ds, fragment sizes reflect joint spacing, with stepped mass distributions corresponding to the imposed discontinuity planes;

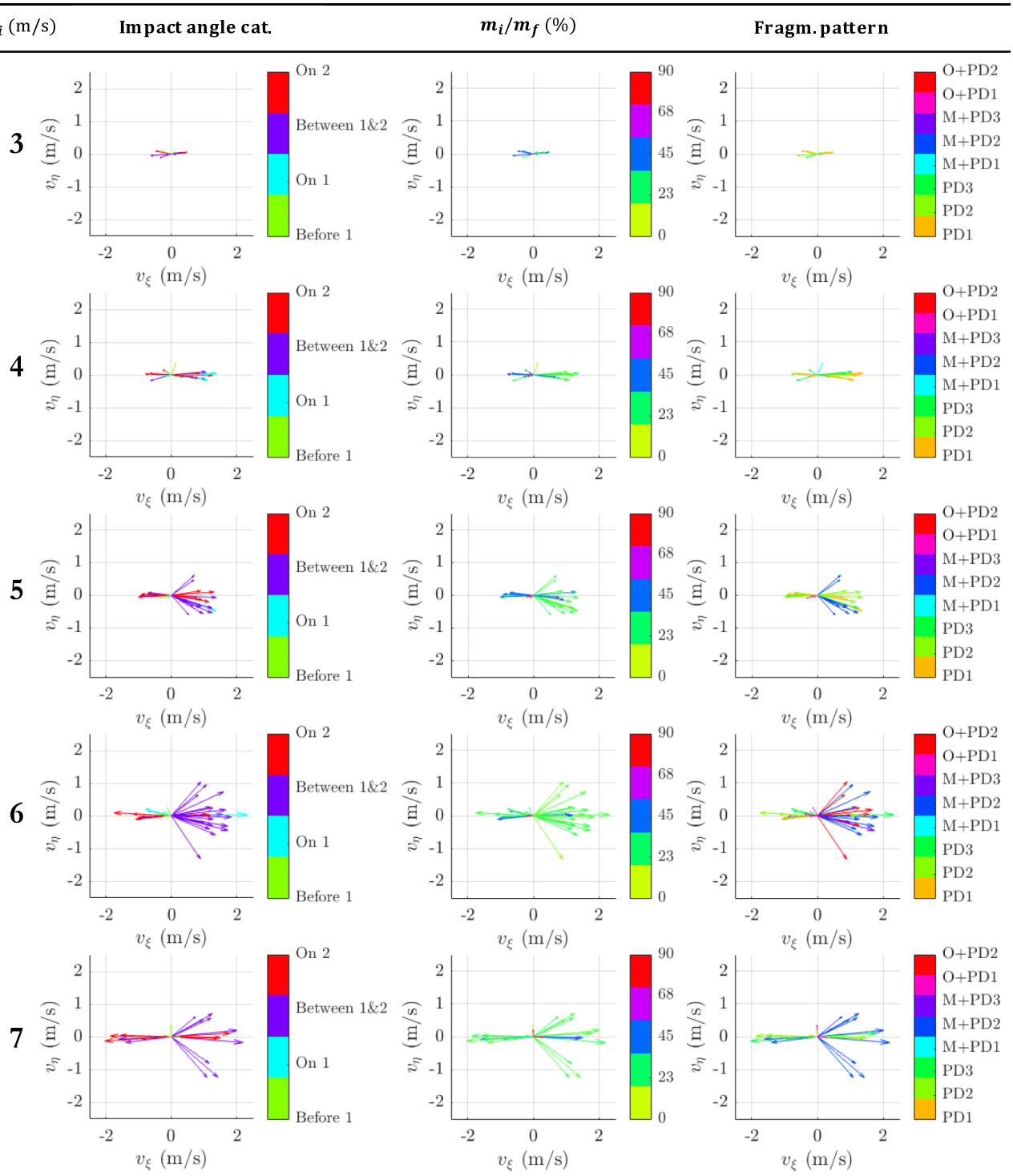

Fig. 22 Post-impact velocity vectors of the fragments for the 3Ds series, for all the velocities, in the $\xi - \eta$ plane, subdivided according to impact angle category (left column), mass of the fragments (middle column), and type of fracture (right column). Each row corresponds to an impact velocity v_i

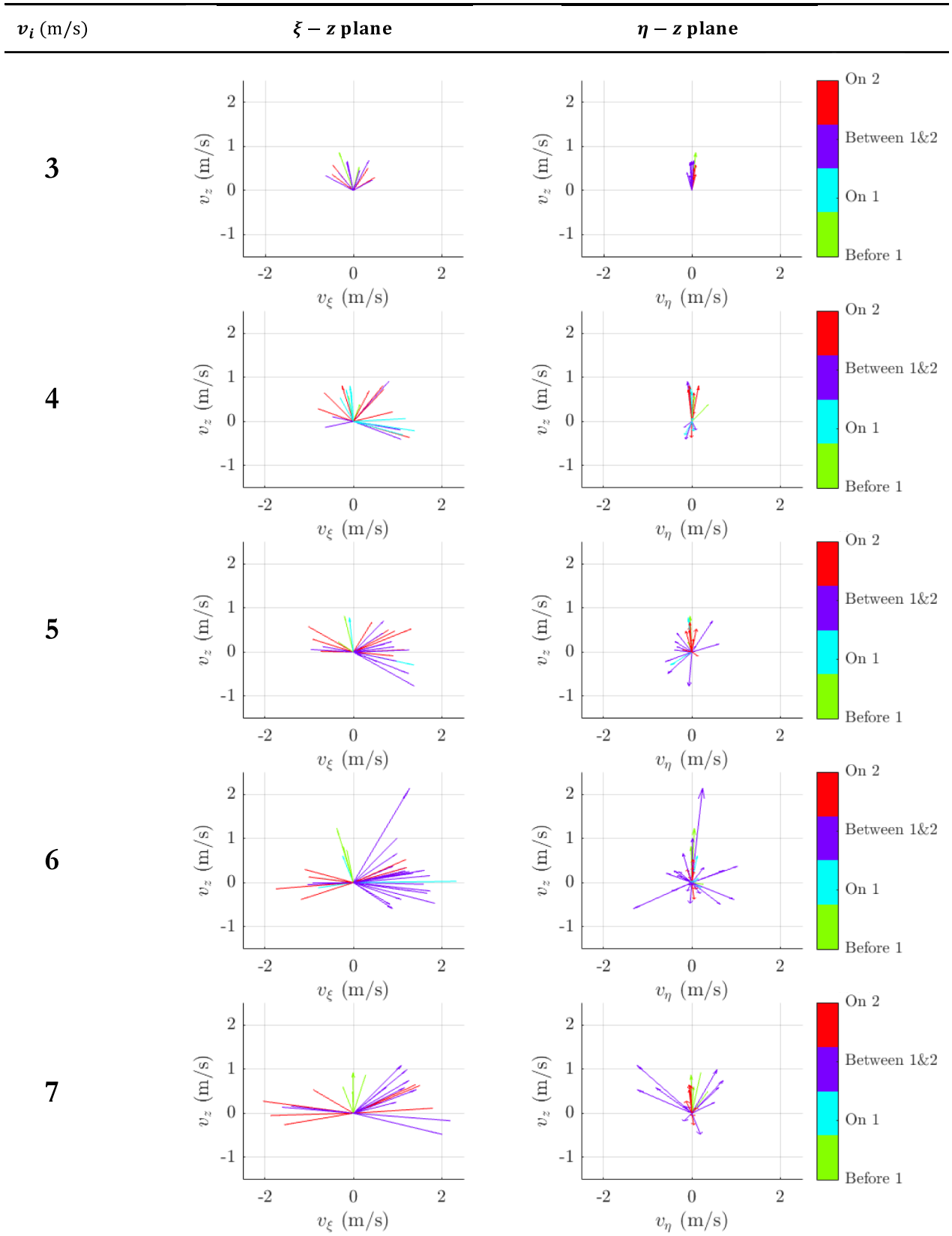

Fig. 23 Post-impact velocity vectors of the fragments for the 3Ds series, for all the velocities, in the $\xi - z$ and $\eta - z$ planes subdivided according to impact angle category. Each row corresponds to an impact velocity v_i

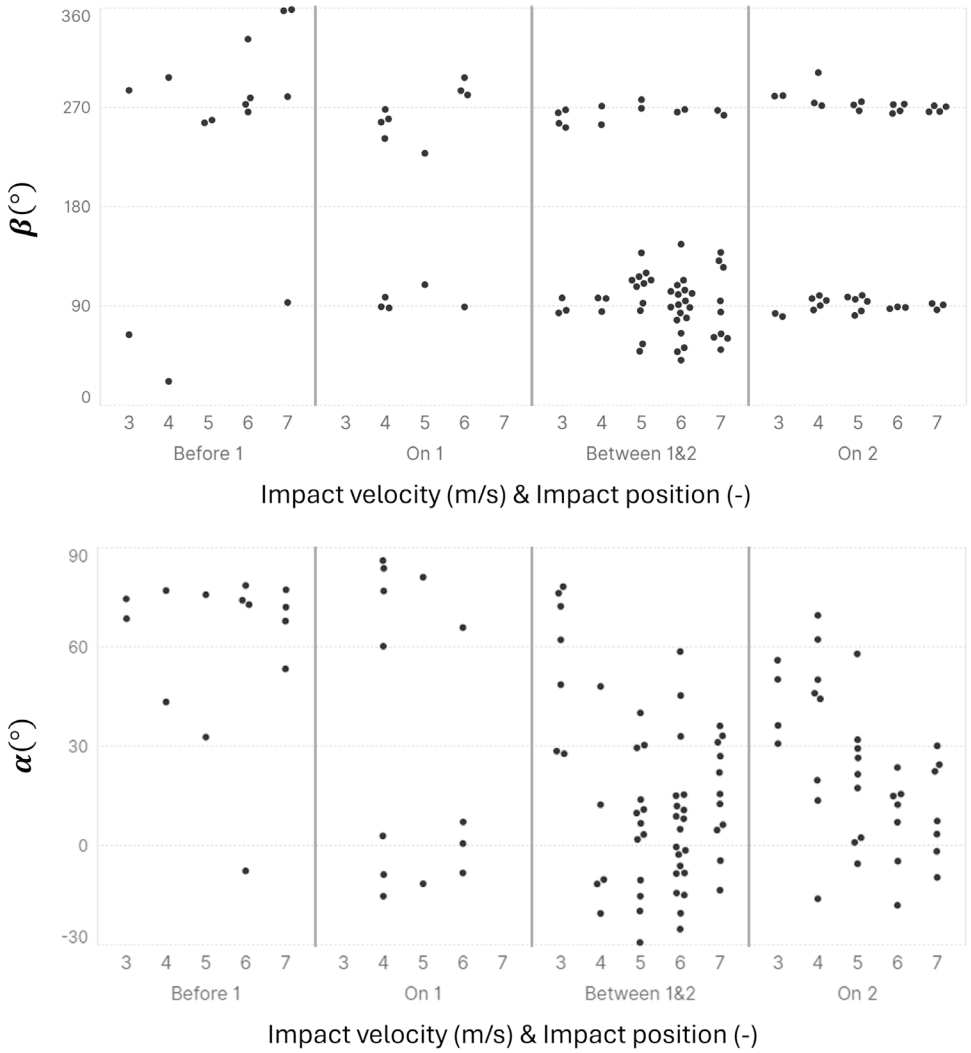

Fig. 24 β and α angles for all fragments as a function of impact angle category and impact velocity for the 3Ds series

- fragment trajectories are governed by both v_i and discontinuity orientation. At $v_i < 7$ m/s, fragments tend to follow the normal to the discontinuity plane, with fan-like dispersion increasing with velocity. At 8.5 10 m/s, fragments are ejected in all directions. This broader dispersion is associated with the onset of fragmentation within the intact matrix, in addition to failure along discontinuities. Vertical rebounds are observed in specific configurations (e.g., 1–4Ds at 45*b*°, 3Ds 'Before 1' and 'On 1');
- a clear positive correlation exists between v_i and the horizontal post-impact velocity components, while the vertical component v_z shows weaker dependence. The normal restitution coefficient $\frac{|v_z|}{|v_i|}$ remains below 0.3 and is unaffected by impact angle, whereas $\frac{|v_f|}{|v_i|}$ is more sensitive to impact angle and generally remains below 0.4;
- from an energy perspective, central discontinuity maximizes energy dissipation and fracture surface.

These findings have direct implications for rockfall hazard assessment and mitigation design. The observed relationships between discontinuity geometry, impact conditions, and fragmentation behaviour provide a physical basis for improving rockfall trajectory models, highlighting the limitations of deterministic trajectory models and support the

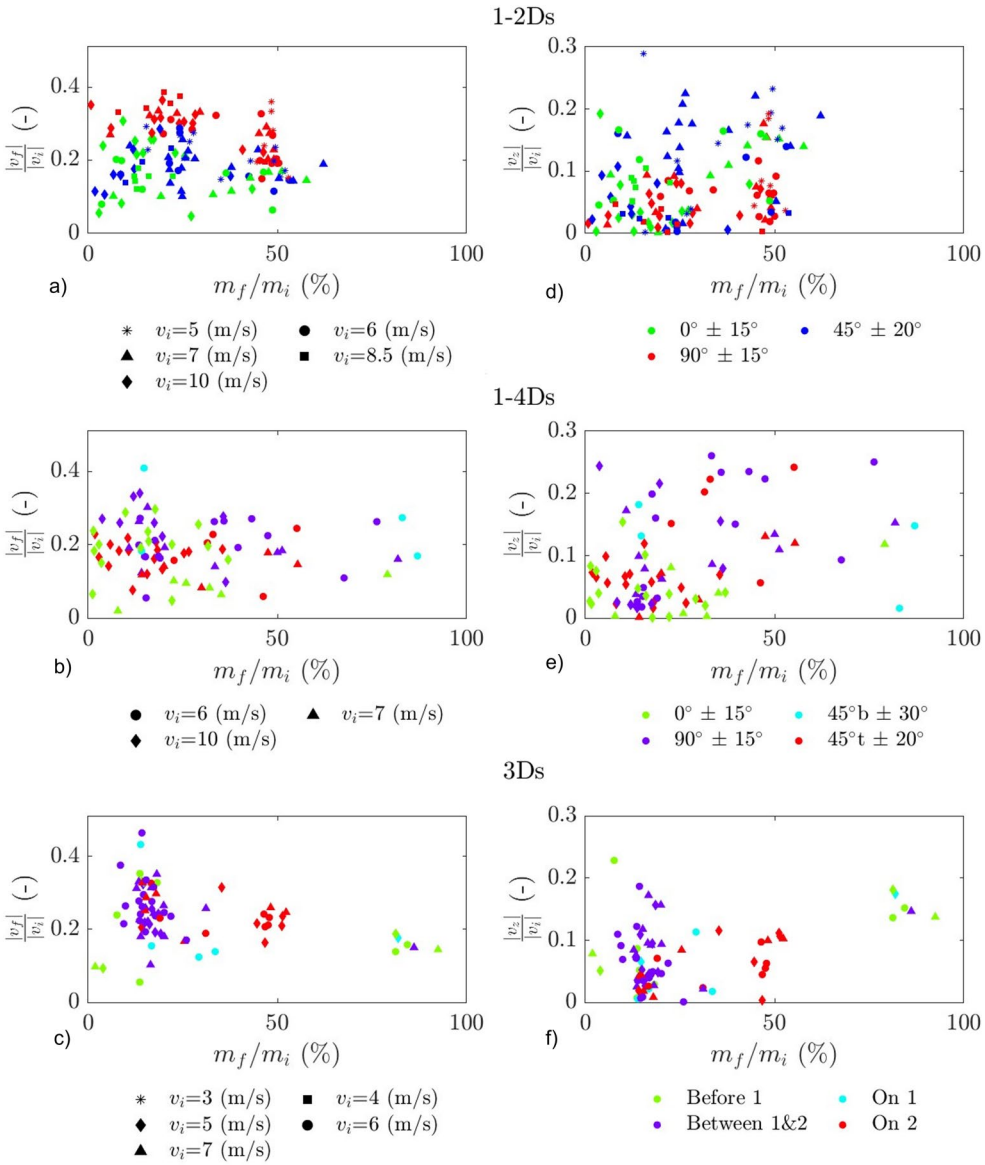

Fig. 25 Ratio of fragment velocity to impact velocity as a function of normalized fragment mass for all series. Left column (**a**–**c**): Total fragment velocity magnitude ($|v_f|/|v_i|$) vs. m_f/m_i. Right column (**d**–**f**): Vertical component of fragment velocity ($|v_z|/|v_i|$) vs. m_f/m_i. Each row corresponds to a different discontinuity(ies) pattern series

use of probabilistic approaches. In particular, the results support the development of probabilistic models where trajectory dispersion increases with impact energy, and fragment mass distributions reflect the presence, geometry, and persistence of discontinuities, e.g., volume bounded by joints in high-density cases, or spacing and impact position in single-joint configurations. Predicting dispersion, jump height, and energy is essential for accurately assessing element vulnerability, forecasting rockfall consequences, and designing effective barriers capable of

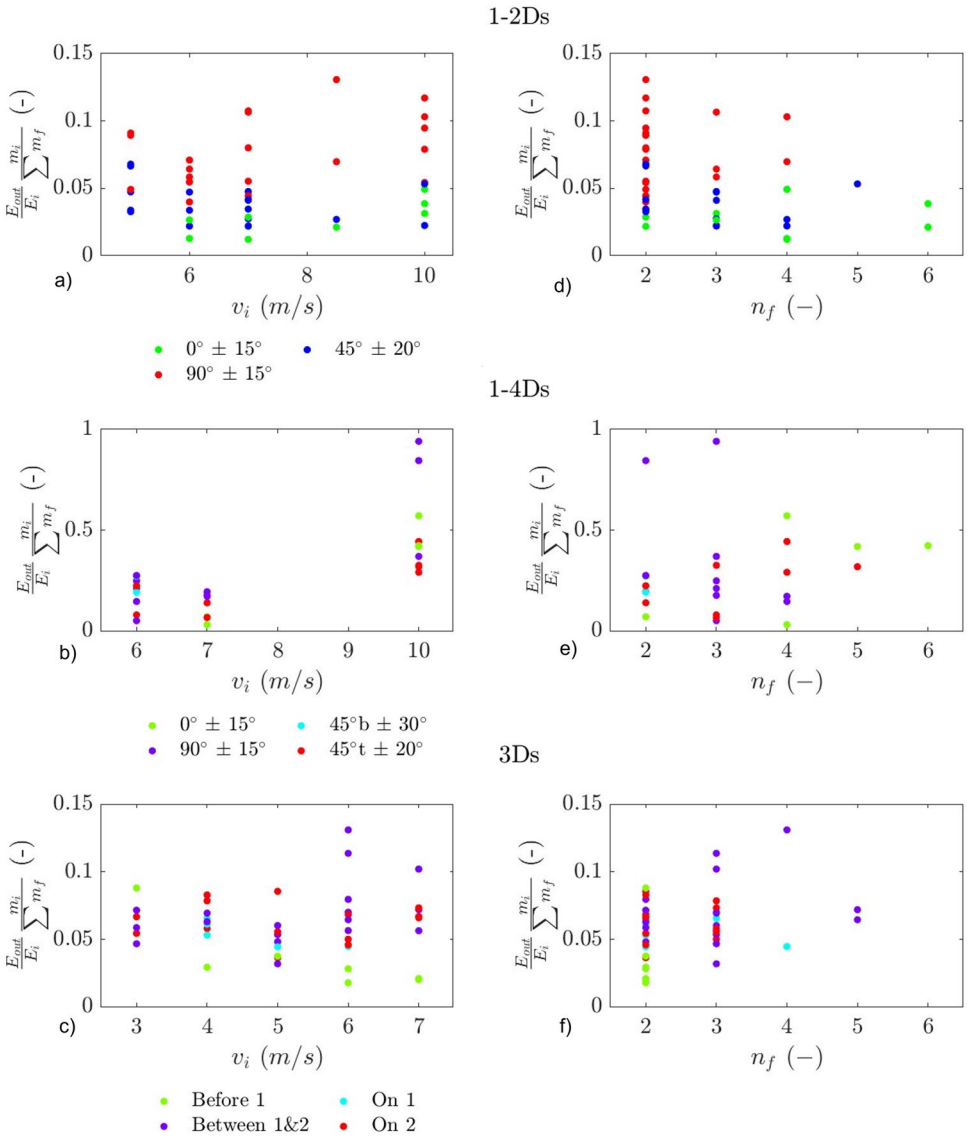

Fig. 26 Ratio of fragments' kinetic energy to impact kinetic energy, scaled by the mass of bouncing fragments only, as a function of impact velocity for all series (left column: **a**–**c**), and as a function of the number of fragments for all series (right column: **d**–**f**). Each row corresponds to a discontinuity(ies) pattern series

intercepting and stopping falling blocks (Marchelli et al. 2020, 2024). Further analyses will be conducted with more realistic shapes and non-collinear impacts.

Acknowledgements The help received from Dr. Michele Spadari, Elena Cozacenco and Wesley Murphey in preparing the samples and conducting the experiments is also gratefully acknowledged.

Author Contributions MM: Conceptualization, Methodology, Laboratory tests, Investigation, Data creation, Formal analyses, Writing-original draft, Writing - Review & Editing, Project administration, Funding acquisition. DEG: Conceptualization, Methodology, Laboratory tests, Writing - Review & Editing, Project administration, Funding acquisition. AG: Conceptualization, Writing - Review & Editing, Supervision, Project administration, Funding acquisition. OB: Conceptualization, Writing - Review & Editing, Supervision, Project administration, Funding acquisition. All authors read and approved the final manuscript.

Funding Open access funding provided by Politecnico di Torino within the CRUI-CARE Agreement. This work was supported by Marie Curie Postdoctoral Fellowship 2022 (Call Horizon-MSCA-2022-PF-01, grant GA101103401 - RIDETHERISK project), by Australian Research Council (IE230100410, DP210101122 and DP160103140) and Rocscience Inc.

Data Availability Data supporting the findings of this study are available from the authors on request.

Declarations

Conflict of interest The authors declare that there is no conflict of interest.

References

Arbiter N (1969) Single fracture of brittle spheres. Soc Min Eng AIME Trans 244:118–133

Asteriou P, Tsiambaos G (2018) Effect of impact velocity, block mass and hardness on the coefficients of restitution for rockfall analysis. Int J Rock Mech Min Sci 106:41–50

Azadmehr A, Jalali SME, Pourrahimian Y (2019) An application of rock engineering system for assessment of the rock mass fragmentation: a hybrid approach and case study. Rock Mech Rock Eng 52(11):4403–4419

Azizi A, Moomivand H (2021) A new approach to represent impact of discontinuity spacing and rock mass description on the median fragment size of blasted rocks using image analysis of rock mass. Rock Mech Rock Eng 54:2013–2038

Aziznejad S, Esmaieli K, Hadjigeorgiou J et al. (2018) Responses of jointed rock masses subjected to impact loading. J Rock Mech Geotechnical Eng 10(4):624–634

Bieniawski Z, Hawkes I (1978) Suggested methods for determining tensile strength of rock materials. Int J Rock Mech Min Sci 15(3):99–103

Bieniawski Z, Bernede M (1979) Suggested methods for determining the uniaxial compressive strength and deformability of rock materials: Part 1. suggested method for determining deformability of rock materials in uniaxial compression. In: International journal of rock mechanics and mining sciences & geomechanics abstracts, Elsevier, pp 138–140

Blahůt J, Racek O (2023) Modern methods of rock mass characterisation and rockfall monitoring: A review. Landslides: Detection, Prediction and Monitoring: Technological Developments pp 1–38

Butcher C, Fityus S, Giacomini A, et al. (2021) The effect of impact angle and bond strength on fragmentation in laminated materials. In: IOP Conference Series: Earth and Environmental Science, ISRM-EUROCK, p 012021

Buzzi O, Guccione DE (2023) An analytical model to predict the survival probability of irregular brittle rocks in rockfall under collinear impact. Rock Mech Rock Eng 56(6):4659–4665

Buzzi O, Ye Y, Vidler A (2024) Numerical study of damage accumulation in brittle spheres during repeated impacts and development of a conceptual model for rocks. Rock Mechanics and Rock Engineering pp 1–22

Carmona HA, Wittel FK, Kun F et al. (2008) Fragmentation processes in impact of spheres. Phys Rev E-Stat Nonlinear Soft Matter Phys 77(5):051302

Corominas J, Mavrouli O, Ruiz-Carulla R (2017) Rockfall occurrence and fragmentation. In: Advancing Culture of Living with Landslides: Volume 1 ISDR-ICL Sendai Partnerships 2015-2025, Springer, pp 75–97

Crosta G, Agliardi F (2003) A methodology for physically based rockfall hazard assessment. Nat Hazard 3(5):407–422

De Biagi V (2017) Brief communication: accuracy of the fallen blocks volume-frequency law. Nat Hazard 17(9):1487–1492

De Blasio FV, Crosta GB (2015) Fragmentation and boosting of rock falls and rock avalanches. Geophys Res Lett 42(20):8463–8470

Dorren L, Schaller C, Erbach A et al. (2023) Automated delimitation of rockfall hazard indication zones using high-resolution trajectory modelling at regional scale. Geosciences 13(6):182

Ferrari F, Giacomini A, Thoeni K (2016) Qualitative rockfall hazard assessment: a comprehensive review of current practices

Frattini P, Crosta G, Agliardi F, et al. (2012) Rockfall characterization and modeling. In: Landslides types, mechanisms and modeling. Cambridge University Press, p 267–281

Giacomini A, Buzzi O, Renard B et al. (2009) Experimental studies on fragmentation of rock falls on impact with rock surfaces. Int J Rock Mech Min Sci 46(4):708–715

Giacomini A, Thoeni K, Santise M et al. (2020) Temporal-spatial frequency rockfall data from open-pit highwalls using a low-cost monitoring system. Remote Sensing 12(15):2459

Gili J, Ruiz-Carulla R, Matas G et al. (2022) Rockfalls: analysis of the block fragmentation through field experiments. Landslides 19(5):1009–1029

Gili J, Ruiz R, Matas G, et al. (2018) Experimental study on rockfall fragmentation: In situ test design and first results. In: landslides and engineered slopes. Experience, theory and practice. CRC Press, p 983–990

Graber A, Santi P (2022) Power law models for rockfall frequency-magnitude distributions: review and identification of factors that influence the scaling exponent. Geomorphology 418:108463

Guccione DE, Buzzi O, Thoeni K et al. (2021a) Predicting the fragmentation survival probability of brittle spheres upon impact from statistical distribution of material properties. Int J Rock Mech Min Sci 142:104768

Guccione DE, Thoeni K, Fityus S et al. (2021b) An experimental setup to study the fragmentation of rocks upon impact. Rock Mech Rock Eng 54(8):4201–4223

Guccione DE, Giacomini A, Thoeni K et al. (2023) On the dynamic fragmentation of rock-like spheres: insights into fragment distribution and energy partition. Rock Mech Rock Eng 56(2):847–873

Han D, Yang H (2021) Effects of tensile stresses on wave propagation across stylolitic rock joints. Int J Rock Mech Min Sci 139:104617

Han D, Zhu J, Leung YF (2022) Failure strength and fracture characteristics of rock with discontinuity under indirect tension. J Rock Mech Geotechnical Eng 14(6):1810–1822

Hantz D, Corominas J, Crosta GB et al. (2021) Definitions and concepts for quantitative rockfall hazard and risk analysis. Geosciences 11(4):158

Jaccard CJ, Abbruzzese JM, Howald EP (2020) An evaluation of the performance of rock fall protection measures and their role in hazard zoning. Nat Hazards 104(1):459–491

Khanal M, Schubert W, Tomas J (2004) Ball impact and crack propagation-simulations of particle compound material. Granular Matter 5(4):177–184

Khanal M, Schubert W, Tomas J (2004b) Crack analysis in single plate stressing of particle compounds. In: Computational Science-ICCS 2004: 4th International Conference, Kraków, Poland, June 6-9, 2004, Proceedings, Part II 4, Springer, pp 364–371

Kuruppu MD, Obara Y, Ayatollahi MR et al. (2014) Isrm-suggested method for determining the mode i static fracture toughness using semi-circular bend specimen. Rock Mech Rock Eng 47:267–274

Lanfranconi C, Frattini P, Sala G et al. (2023) Accounting for the effect of forest and fragmentation in probabilistic rockfall hazard. Nat Hazard 23(6):2349–2363

Lanfranconi C, Frattini P, Agliardi F et al. (2024) Field evidence and indicators of rockfall fragmentation and implications for mobility. Eng Geol 341:107704

Leine RI, Schweizer A, Christen M et al. (2014) Simulation of rockfall trajectories with consideration of rock shape. Multibody SysDyn 32:241–271

Li L, Lan H (2015) Probabilistic modeling of rockfall trajectories: a review. Bull Eng Geol Env 74:1163–1176
Lin Q, Cheng Q, Li K, et al. (2020) Contributions of rock mass structure to the emplacement of fragmenting rockfalls and rockslides: insights from laboratory experiments. Journal of Geophysical Research: Solid Earth 125(4):e2019JB019296
Liu L, Kafui K, Thornton C (2010) Impact breakage of spherical, cuboidal and cylindrical agglomerates. Powder Technol 199(2):189–196
Liu B, He K, Han M et al. (2021) Dynamic process simulation of the xiaogangjian rockslide occurred in shattered mountain based on 3dec and dfn. Comput Geotech 134:104122
Marchelli M, De Biagi V (2019) Optimization methods for the evaluation of the parameters of a rockfall fractal fragmentation model. Landslides 16(7):1385–1396
Marchelli M, Biagi VD, Peila D (2020) Reliability-based design of protection net fences: influence of rockfall uncertainties through a statistical analysis. Geosciences 10(8):280
Marchelli M, Coltrinari G, Degan GA et al. (2023) Towards a procedure to manage safety on construction sites of rockfall protective measures. Saf Sci 168:106307
Marchelli M, De Biagi V, Bertolo D, et al. (2022) A mixed quantitative approach to evaluate rockfall risk and the maximum allowable traffic on road infrastructure. Georisk: Assessment and Management of Risk for Engineered Systems and Geohazards 16(3):584–594
Marchelli M, De Biagi V, Chiaia B (2024) A fully probabilistic framework to compute the residual rockfall risk in presence of mitigation measures. Landslides pp 1–8
Matas G, Lantada N, Corominas J et al. (2017) Rockgis: a gis-based model for the analysis of fragmentation in rockfalls. Landslides 14(5):1565–1578
Matas G, Lantada N, Corominas J et al. (2020) Simulation of full-scale rockfall tests with a fragmentation model. Geosciences 10(5):168
Mavrouli O, Corominas J, Jaboyedoff M (2015) Size distribution for potentially unstable rock masses and in situ rock blocks using lidar-generated digital elevation models. Rock Mech Rock Eng 48:1589–1604
Moos C, Bontognali Z, Dorren L et al. (2022) Estimating rockfall and block volume scenarios based on a straightforward rockfall frequency model. Eng Geol 309:106828
Noël F, Jaboyedoff M, Caviezel A et al. (2022) Rockfall trajectory reconstruction: a flexible method utilizing video footage and high-resolution terrain models. Earth Surf Dyn Discuss 2022:1–30
Prades-Valls A, Corominas J, Lantada N et al. (2022) Capturing rockfall kinematic and fragmentation parameters using high-speed camera system. Eng Geol 302:106629
Rosser N, Massey C (2022) Rockfall hazard and risk. In: Landslide Hazards, Risks, and Disasters. Elsevier, p 581–622
Ruiz-Carulla R, Corominas J (2020) Analysis of rockfalls by means of a fractal fragmentation model. Rock Mech Rock Eng 53(3):1433–1455
Ruiz-Carulla R, Corominas J, Mavrouli O (2017) A fractal fragmentation model for rockfalls. Landslides 14(3):875–889
Ruiz-Carulla R, Corominas J, Gili JA et al. (2020) Analysis of fragmentation of rock blocks from real-scale tests. Geosciences 10(8):308
Ruiz-Carulla R, Matas G, Corominas J, et al. (2021) 3d analysis of a fragmental rockfall. Understanding and Reducing Landslide Disaster Risk: Volume 4 Testing, Modeling and Risk Assessment 5th pp 187–194
Salman A, Reynolds G, Hounslow M (2003) Particle impact breakage in particulate processing. Kona Powder Part J 21:88–99
Salman A, Reynolds G, Fu J et al. (2004) Descriptive classification of the impact failure modes of spherical particles. Powder Technol 143:19–30
Scavia C, Barbero M, Castelli M et al. (2020) Evaluating rockfall risk: some critical aspects. Geosciences 10(3):98
Shang J, Hencher S, West L (2016) Tensile strength of geological discontinuities including incipient bedding, rock joints and mineral veins. Rock Mech Rock Eng 49:4213–4225
Shipway P, Hutchings I (1993) Attrition of brittle spheres by fracture under compression and impact loading. Powder Technol 76(1):23–30
Shipway P, Hutchings I (1993b) Fracture of brittle spheres under compression and impact loading. i. elastic stress distributions. Philosophical Magazine A 67(6):1389–1404
TEMA (2019) Image systems motion analysis, TEMA 3D. http://www.imagesystems.se/tema/
The MathWorks Inc. (2023) Matlab version: 9.13.0 (r2023b). https://www.mathworks.com
Tomas J, Schreier M, Gröger T et al. (1999) Impact crushing of concrete for liberation and recycling. Powder Technol 105(1–3):39–51
Wang Y, Tonon F (2011) Discrete element modeling of rock fragmentation upon impact in rock fall analysis. Rock Mech Rock Eng 44:23–35
Wang Y, Tonon F (2011) Dynamic validation of a discrete element code in modeling rock fragmentation. Int J Rock Mech Min Sci 48(4):535–545
Williams JG, Rosser NJ, Hardy RJ et al. (2019) The importance of monitoring interval for rockfall magnitude-frequency estimation. J Geophys Res Earth Surf 124(12):2841–2853
Wittel FK, Carmona HA, Kun F et al. (2008) Mechanisms in impact fragmentation. Int J Fract 154:105–117
Wu S, Chau KT, Yu T (2004) Crushing and fragmentation of brittle spheres under double impact test. Powder Technol 143:41–55
Wu N, Zhu Z, Zhang C et al. (2019) Dynamic behavior of rock joint under different impact loads. KSCE J Civ Eng 23:541–548
Wu M, Luo G, Hu X et al. (2025) Dynamic fragmentation analysis of potential rockfall hazards at zixia hydropower dam, qinghai-tibet plateau. J Rock Mech Geotechnical Eng 17:4109–4123
Wyllie DC (2014) Calibration of rock fall modeling parameters. Int J Rock Mech Min Sci 67:170–180
Xu H, Zhang Z, Yan J et al. (2024) Study on mechanical properties and failure mechanism of hard rock with stiff discontinuities based on 3d printing. Eng Fail Anal 161:108225
Ye Y, Thoeni K, Zeng Y et al. (2019) A novel 3d clumped particle method to simulate the complex mechanical behavior of rock. Int J Rock Mech Min Sci 120:1–16
Ye Y, Zeng Y, Cheng S et al. (2021) Numerical investigation of rock sphere breakage upon oblique impact: effect of the contact friction coefficient and impact angle. Comput Geotech 136:104207
Zhao T, Crosta GB, Utili S et al. (2017) Investigation of rock fragmentation during rockfalls and rock avalanches via 3-d discrete element analyses. J Geophys Res Earth Surf 122(3):678–695